Clear-Sky Criteria and Cloud Cover over Desert Areas from Meteosat Data

MICHEL CAPDEROU AND ROBERT KANDEL

Laboratoire de Météorologie Dynamique du CNRS, Ecole Polytechnique, Palaiseau, France

(Manuscript received 22 October 1992, in final form 24 September 1993)

ABSTRACT

In order to use the diurnal variation of Meteosat visible channel data to help determine the bidirectional reflectance function for desert areas, criteria must be established for identifying cloud-free scenes. The authors consider Meteosat observations, obtained in different seasons over four years, of desert and arid land areas of Africa and the Arabian peninsula. Normalizing apparent albedo to near-midday values, the authors show that clear and cloudy scenes can be distinguished using relative spatial heterogeneity parameters of this normalized albedo on the one hand, and of the midday infrared window radiance on the other. Further, it is shown that cloud cover estimates based on these parameters are in good agreement with the C1 results of the International Satellite Cloud Climatology Project. Difficulties related to Saharan dust clouds or to homogeneous overcast cases can be resolved by comparing midday IR window radiance with the maximum value over a 10-day period.

1. Introduction

The components of the earth radiation budget at the top of the atmosphere (TOA) can only be observed from space, but information on regional scales smaller than a thousand kilometers can only be extracted by converting radiance measurements made with narrow-field-of-view instruments (e.g., scanning radiometers) into radiant exitance (flux). Albedo determinations are particularly delicate, because the bidirectional reflectance properties of the earth–atmosphere are strongly anisotropic (non-Lambertian) in many cases, depending both on the cloud cover and the nature of the underlying surface. We recall that for solar zenith angle θ_o, the TOA albedo $a(\theta_o)$ is given by

$$a(\theta_o) = \frac{M_{SW}(\theta_o)}{E \cos\theta_o}. \tag{1}$$

Here E is the TOA normal solar irradiance, that is, the solar constant corrected for the earth–sun distance at the date of observation, and M_{SW}, the reflected shortwave (SW) flux, is an integration of reflected radiances L_{SW} over viewing zenith angle θ and relative sun–target–observer azimuth ϕ in the outgoing hemisphere:

$$M_{SW}(\theta_o) = \int_{\phi=0}^{2\pi} \int_{\theta=0}^{\pi/2} L_{SW}(\theta_o, \theta, \phi) \cos\theta \sin\theta d\theta d\phi. \tag{2}$$

The shortwave anisotropic function is given by

$$R(\theta_o, \theta, \phi) = \frac{\pi L_{SW}(\theta_o, \theta, \phi)}{M_{SW}(\theta_o)}, \tag{3}$$

and it is equal to 1 for Lambertian reflection, that is, reflected radiance independent of viewing angles θ and ϕ.

In the Earth Radiation Budget Experiment (ERBE), SW radiance-to-flux conversion was carried out (Smith et al. 1986; Wielicki and Green 1989) using values of R tabulated for different scene types (Suttles et al. 1988). These values were derived mainly by combining measurements made at different viewing angles θ and ϕ with the rotating azimuth ERB scanner on board *Nimbus-7*. For this sun-synchronous satellite orbit, all the measurements are close to local noon, so that for underlying scene types such as desert, which occur only in certain latitude bands, only a restricted range of solar zenith angles can be sampled. Geostationary satellites can provide a complete range of solar zenith angles, although at the price of restricting the viewing angles. Some use was made of Geostationary Operational Environmental Satellite (GOES) data in deriving the tables of R, but it should be noted that the deserts observed by GOES are limited in extent and that their bidirectional reflectance may be perturbed by effects of relief. By contrast, most of the world's desert area is observed by Meteosat and relief effects should on the whole be smaller.

It therefore is desirable to use the more complete solar zenith angle sampling of Meteosat data to verify and if necessary correct the bidirectional reflectance functions for desert scenes. This can be done by analyzing the diurnal variation of the reflected SW radiance for clear desert scenes. A necessary first step is the definition of criteria for choosing desert scenes that remain

Corresponding author address: Michel Capderou, Laboratoire de Météorologie Dynamique du CNRS, Ecole Polytechnique, F-91128, Palaiseau, France.

cloud-free during an entire day. In section 2, we define a "normalized" albedo and other parameters that are useful for this purpose. We examine the distributions of these parameters over different arid regions and during different seasons in section 3. We compare the clear-sky and cloud cover determinations that we obtain from our Meteosat parameters, with results of the International Satellite Cloud Climatology Project (ISCCP) in section 4. Results are discussed in the concluding section.

2. Meteosat parameters for diurnal BDRF and cloud analyses

a. Bidirectional reflectance function (BDRF)

In each channel n, the satellite transmits a signal (8-bit count) C_n that is proportional (after subtraction of the offset C_{0n}) to the observed radiance L_n (W m^{-2} sr^{-1}) as filtered by the channel spectral response function. We can write

$$L_n = K_n(C_n - C_{0n}) \tag{4}$$

where the offset C_{0n} can be determined for the visible channel (VIS) by measurements at night and for the IR window channel by space looks. The Meteosat VIS channel response extends over a broad wavelength range (0.4–1.2 μm) and is not flat. The conversion coefficient K_{VIS} therefore depends on the spectral distribution of the scene albedo (Koepke 1982; Stum 1985) but leaving aside the case of clear (and therefore blue) ocean, it is fairly insensitive to the scene type (Courel et al. 1984). Calculations using the 5S SW radiative transfer code (Tanré et al. 1990) show that it also remains insensitive to viewing conditions for relatively bright scenes observed within 60° of nadir. In our work we have retained the value $K_{VIS} = 1.58$ W m^{-2} sr^{-1} per 8-bit count from Koepke (1983), which is used in the 5S code. For the most part, however, we use relative values of VIS and IR radiances in this work, so that the absolute numerical value of K_n is irrelevant.

Omitting the offset term and channel indices n to simplify the notation, and neglecting the difference between the Meteosat VIS channel and a true SW channel with flat response from 0.2- to 4-μm wavelength, we write the "apparent albedo" sensed by Meteosat as

$$\rho = aR = \frac{\pi KC}{E\cos\theta_o}, \tag{5}$$

which is the product of the intrinsic albedo $a(\theta_o)$ and the normalized shortwave anisotropic function $R(\theta_o, \theta, \phi)$. This value $\rho(\theta_o, \theta, \phi)$ is a bidirectional reflectance function (BDRF). To obtain the intrinsic albedo, which is the quantity of interest in earth radiation budget studies, we need to choose the BDRF, which depends strongly on the scene type and especially on the cloud cover. In order to use observations to improve the BDRF for a given scene type and cloud cover class, we must be able to discriminate accurately between clear and cloudy scenes. Similarly, accurate clear-/cloudy-sky criteria are needed in order to choose the right BDRF for converting radiance measurements into flux and albedo estimates, and also for the determination of cloud radiative forcing.

b. Meteosat data used

The Meteosat full-resolution images are 2500-pixel × 2500-pixel grids, with one image each half hour. At the subsatellite point (0°, 0°), one pixel represents a 5-km × 5-km square (the original 2.5-km resolution of the VIS measurement is sampled to 5 km).

The ISCCP B2 images (B2) (Schiffer and Rossow 1983) are obtained by sampling one line on six (the 6th), one pixel on six (the 6th), one image on six (image start time: 0230, 0530, . . . , 1130, . . . , 2330 UTC). Thus, we dispose of one image every 3 h, with a 416-pixel × 416-pixel grid: one B2 pixel represents a 30-km × 30-km square at the subsatellite point.

The VIS channel has a roughly triangular response, between 0.4 μm and 1.1 μm, with a maximum at 0.75 μm. The measurements are made with a radiometric resolution of 64 levels (counts), that is, on six bits. On the tape, the records are converted into 256 levels, that is, on 8 bits (for *Meteosat-4*, direct record on 256 levels). The IR channel has a response between 10.2 and 12.8 μm, with a maximum from 11 to 12 μm. The measurements are made with a radiometric resolution of 256 levels.

For this study, we have used the B2 VIS and IR data for all the days of the following months: the 12 months of the year 1985; and the months January and July for different years between 1983 and 1990. All data are from *Meteosat-2* (except for 1990: *Meteosat-4*).

The exact instant of observation (pixel acquisition) is perfectly determined by the image "time slot" and by the pixel's geographical position (Table 1), considering the fact that the radiometer scans 100 lines per minute. We note that for a particular geographical target area the viewing zenith angle θ is fixed, but the solar zenith angle θ_o and the relative azimuth ϕ are varying.

c. Reflectance ratio (BDRF ratio)

For a single pixel or group of pixels, we obtain the BDRF ρ_i for each time slot i. To eliminate the problem

TABLE 1. Image start–stop times (full earth scan).

Time slot i	Image start–stop times (UTC)
3	0530–0555
4	0830–0855
5	1130–1155
6	1430–1455
7	1730–1755

of channel calibration, instead of the bidirectional reflectance functions we consider normalized values. An ideal reference would be the BDRF for the sun at zenith, but this situation is very rare or nonexistent depending on the latitude and date. We consider a time slot c for which the observation is closest to local noon, and we define the BDRF ratio as

$$D_i = \frac{\rho_i}{\rho_c} = \frac{C_i}{C_c}\frac{\cos\theta_{oc}}{\cos\theta_{oi}}. \qquad (6)$$

We note that this quantity is by definition equal to 1 for time slot $i = c$. In order to simplify the expression, we have omitted the index $n = 1$ corresponding to the visible channel in the expression of signal C (8-bit count).

The solar zenith angle at the central time slot, θ_{oc}, stays less than 40° all year for the areas studied, except for the northern part of the Sahara and the Arabian Desert where it approaches 50° in the winter. The dependence of albedo on solar zenith angle remains very small from zenith to 36° [bins 1 and 2 in the ERBE angular model tabulation of Suttles et al. (1988)]. Thus we expect that normalization to the central slot provides a good basis for comparison even if the central solar zenith angle is not identical from one region or season to another. We neglect the influence of diurnal change in the spectral composition of the reflected radiation, convoluted with the Meteosat VIS spectral response function, as noted above. This becomes significant only for darker scenes observed at zenith angles greater than 60°.

d. *Analysis of Meteosat areas*

We have analyzed a total of 42 areas approximately 450 km × 450 km (Fig. 1). These areas are located in four major regions (Table 2) including the Sahara and Arabian Deserts in the Northern Hemisphere, the Namib and Kalahari Deserts in southern Africa, and also the semiarid Sahel zone south of the Sahara, which resembles a desert during the dry season (November–April). The areas typically contain 18 × 21 B2 pixels each; for each of these pixels (line j, column k of a rectangular array) we measure (after subtraction of offsets) VIS and IR signals at time slot i. We further divide each area into subareas of 3 × 3 pixels, and for the central pixel p of each of these, we compute the VIS and IR means of the nine values. Thus, each area is represented by about 40 subareas p roughly 100 km on a side (Fig. 2). Averaging over the nine sampled pixels of a subarea is necessary because we cannot be sure that the sampled individual pixels are found at exactly the same place at different times. Shifts of pixel location combined with surface heterogeneity yield anomalous values of $D_{i,p}$ and $\sigma(D_i)$ over an area (Table 3) even when conditions are known to be clear. A mean on nine pixels reduces the impact of such irregularities; a mean on 25 pixels (~150 km × 150 km) smears out the intrinsic spatial variability and is likely to perturb the estimate of cloud cover fraction (Sèze and Rossow 1991). The subareas of 3 × 3 pixels are named "analysis points."

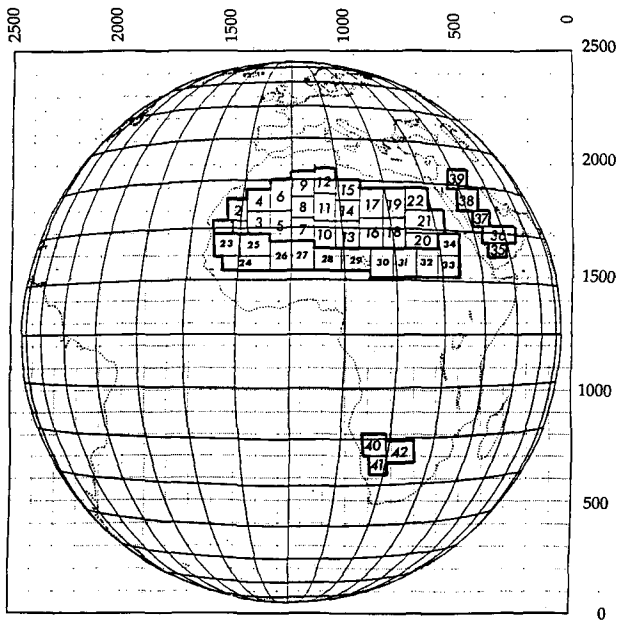

FIG. 1. Geographical zones and areas studied, drawn on Meteosat full resolution (2500 × 2500) grid. Numbers used in the figure to refer to numbers and names in Table 2.

The central time slot is 1130 UTC for the Sahara, Sahel, and Namib–Kalahari, 0830 UTC for the Arabian Desert. For each time slot i, and for each of the analysis points p in an area, we compute the solar and viewing angles. Because of the limited size of the areas 450 km × 450 km, these angles are all practically identical (within ±2°), and in practice we can use the values corresponding to the geometric center of the area. This allows us to compute BDRF (if the conversion coefficient is known) and in any case to compute BDRF ratio $D_{i,p}$ (i: time slot; p: analysis point) by Eq. (6). We can then use these values for the N analysis points of the area, to compute mean values and spatial variability (standard deviation σ). We thus obtain the following quantities for each time slot i on a given day:

BDRF (apparent albedo): mean ρ_i and standard deviation $\sigma(\rho_i)$;
BDRF ratio: mean D_i and standard deviation $\sigma(D_i)$;
IR window count: mean IR_i and standard deviation $\sigma(IR)_i$.

The advantage of the BDRF ratio is that it has no direct dependence on the spatial variations of the surface albedo, while remaining sensitive to temporal variations that depend on the shortwave anisotropic function as well as possible cloud variations.

TABLE 2. Meteosat analysis areas in the four zones studied; for central location of each area, terrestrial coordinates and satellite Meteosat view angles.

Number	Area	Geographic region	Latitude	Longitude	Zenith (°)	Azimuth (°)
	Sahara					
01	Atar	Adrar	20.1°N	12.0°W	27.3	328.3
02	Bir Moghrein	Erg Iguidi	23.6°N	10.7°W	30.1	334.7
03	El Mreyer	Djouf	21.3°N	6.6°W	26.1	342.3
04	Tindouf	Hammada	25.8°N	6.9°W	31.1	344.5
05	Touadeni	Tanezrouft	20.5°N	2.4°W	24.1	353.2
06	Bou Bernous	Erg Chech	26.9°N	2.5°W	31.6	354.5
07	Kidal	Adrar Iforas	19.7°N	2.1°E	23.2	6.1
08	Oualen	Tanezrouft	24.0°N	2.1°E	28.2	5.2
09	Timimoun	Tademait—Gr. Erg	29.1°N	2.2°E	34.1	4.6
10	In Guezzam	Talak	18.5°N	6.4°E	22.9	19.6
11	Tamanrasset	Hoggar	24.2°N	6.7°E	29.3	16.1
12	Ouargla	E. Grand Erg	29.8°N	7.1°E	35.6	14.2
13	Bilma	Tenere	18.5°N	10.6°E	24.9	30.6
14	Ghat	Djado—Fezzan	23.6°N	11.1°E	30.3	26.1
15	Sabha	Hammada el Hamra	28.3°N	11.6°E	35.5	23.4
16	Bardai	Borkou—Tibesti	19.0°N	15.3°E	28.3	40.0
17	Waw an Namus	Libyan Desert	25.1°N	16.1°E	34.4	34.2
18	Fada	Ennedi	19.1°N	20.0°E	32.0	48.1
19	Koufra	Libyan Desert	25.2°N	21.1°E	37.8	42.2
20	El Atrun	Merowe	17.9°N	25.8°E	36.2	57.6
21	El Uweinat	Guilf Kebir	21.7°N	27.1°E	39.8	54.1
22	Farafra	W. Egypt. Desert	26.3°N	26.4°E	42.4	48.2
	Sahel					
23	Tidjikja	Tagant	16.8°N	12.5°W	24.5	322.4
24	Segou	Niger River	13.2°N	8.8°W	18.6	325.7
25	Oualata	Aoukar	16.8°N	7.1°W	21.3	336.8
26	Tombouctou	Niger River	14.7°N	2.3°W	17.4	351.0
27	Menaka	Azaouak	14.7°N	2.0°E	17.4	7.8
28	Tahoua	Tarka	13.9°N	6.7°E	18.1	25.9
29	Nguigmi	Lake Chad	14.0°N	12.0°E	21.5	41.5
30	Koro-Toro	Djourab Erg	13.2°N	16.9°E	25.0	52.9
31	Abeche	Ouaddai	13.3°N	21.5°E	29.4	59.7
32	El Fasher	Darfour	13.4°N	26.4°E	34.3	65.0
33	El Obeid	Kordofan	12.7°N	31.3°E	39.0	70.0
34	Khartoum	Bayuda	17.3°N	32.2°E	41.9	64.7
	Arabian Desert					
35	Tarim	Yemen	16.7°N	46.6°E	56.1	74.8
36	Al Jaladah	Rub el Khali	20.2°N	47.5°E	58.0	72.4
37	Riyadh	Nejd	23.3°N	43.9°E	55.7	67.6
38	Hail	Nejd	27.0°N	41.5°E	55.3	62.8
39	Sakakah	Nafud	31.0°N	40.4°E	56.4	58.8
	Namib-Kalahari					
40	Windhoek	Namib	21.1°S	16.6°E	31.1	140.4
41	Keetmanshoop	Namib	25.5°S	17.6°E	35.7	143.6
42	Gaberones	Kalahari	22.8°S	22.4°E	36.7	133.2

e. Spatial heterogeneity parameters

It is of interest to define additional quantities related to the spatial heterogeneity of the central time slot and observations near noon. These quantities are obtained from the distribution of values used to compute spatial means over an area. The first of these is the normalized standard deviation of the BDRF near noon:

$$s_1 = \frac{\sigma(\rho_c)}{\rho_c}. \quad (7)$$

This is not the same thing as the standard deviation of the BDRF ratio, which we define as follows. At the central time slot, $D_{c,p} = 1$ for all points p, so that $\sigma(D_c) = 0$. We consider the two time slots surrounding the central time slot, thus separated by 6 h, and write

$$s_2 = \frac{1}{2}[\sigma(D_{c-1}) + \sigma(D_{c+1})]. \quad (8)$$

Note that s_2 can be considered as a mean over time of two spatial variances. Finally we also compute the normalized standard deviation of the IR window signal near noon:

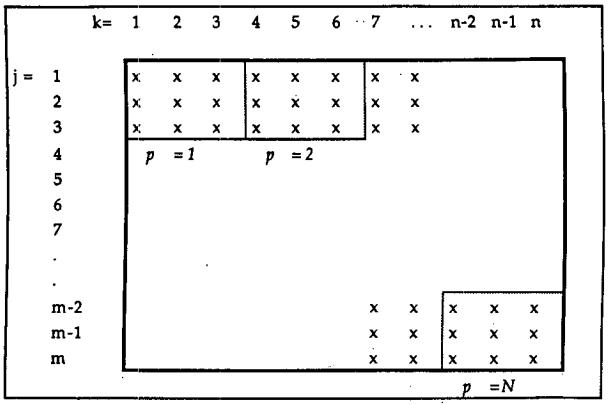

FIG. 2. The B2 pixels (j, k) and analysis points p in an area.

$$s_3 = \frac{\sigma(\mathrm{IR}_c)}{\mathrm{IR}_c}. \quad (9)$$

The auxiliary variables s_1 and s_2 can be interpreted, considering an area containing N points of analysis p, for which a single set of angles (θ_o, θ, ϕ) is adequate to describe the geometry of observation at time slot i. We can write the BDRF defined by Eq. (5) as

$$\rho_{i,p} = \rho_{i,p}(\theta_{oi}, \theta_i, \phi_i) = A_p \alpha(\theta_{oi}) R(\theta_{oi}, \theta_i, \phi_i) \quad (10)$$

for point p at time slot i, where the albedo $a_p(\theta_{oi})$ can be written as the product of the normalized directional albedo function

$$\alpha(\theta_{oi}) = \frac{a_p(\theta_{oi})}{a_p(\theta_o = 0)}$$

and

$$A_p = a_p(\theta_o = 0),$$

which is the albedo of point p for zenith sun, depending on such local characteristics as soil color, vegetation, or cloud cover at the time of observation.

In the ERBE formulation that we follow here, it is assumed that there are different normalized functions $\alpha(\theta_o)$ and $R(\theta_o, \theta, \phi)$ for different scene types, but that a single set applies to all scenes of a given type, for example to all clear desert scenes, even though A_p may vary over a wide range. The real situation is of course more complex, and in fact a variety of angular functions may apply to different scenes, all classified (for example) as partly cloudy desert or land in the ERBE scheme. Using the ERBE formulation, the mean value of the reflectance over an area of N points p of scene type $n(p, i)$ is

$$\rho_i = \langle \rho_{i,p} \rangle = \frac{1}{N} \sum_{p=1}^{N} A[p, n(p, i)] \times \alpha[n(p, i), i] R[n(p, i), i]. \quad (11)$$

TABLE 3. Influence of the size of subarea. Example: 5 July 1985—area 11 (Tamanrasset). BDRF ratio D_i and its variance $\sigma(D_i)$ for time slot $i = c - 1$ and $i = c + 1$, for different size of analysis point.

	Time slot $i = 4$		Time slot $i = 6$	
Subarea size Number of pixels	0848 UTC D_i	0906 LST $\sigma(D_i)$	1448 UTC D_i	1506 LST $\sigma(D_i)$
$1 \times 1 = 1$	0.99	0.14	0.97	0.08
$2 \times 2 = 4$	0.97	0.05	0.96	0.04
$3 \times 3 = 9$	0.97	0.04	0.97	0.03
$4 \times 4 = 16$	0.97	0.04	0.97	0.02
$5 \times 5 = 25$	0.97	0.03	0.97	0.02

Here it should be noted that A depends on i only to the extent that the scene type, that is, the cloud cover, may depend on the time corresponding to slot i; the angular functions depend on i both because of this

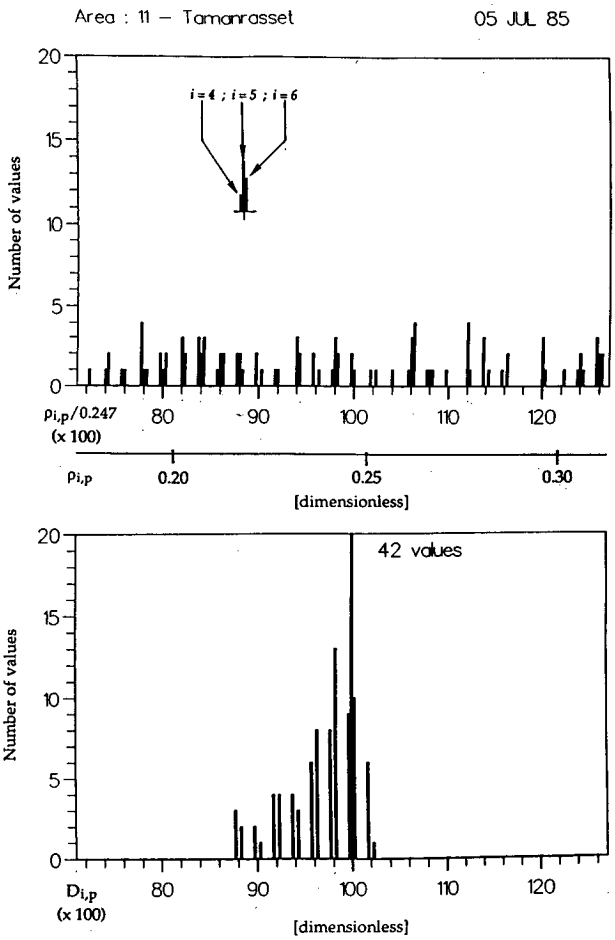

FIG. 3. Albedo histograms, for 42 points of area 11 (Tamanrasset; Sahara zone), 5 July 1985. Time slot $i = 4$, $i = c = 5$, $i = 6$. (a) BDRF (apparent albedo) $\rho_{i,p}$. To compare the distribution length between BDRF and BDRF ratio, the values of $\rho_{i,p}/0.247$ are noted on the same scale as the values of $D_{i,p}$ ($\rho_c = 0.247$ is the mean value of $\rho_{c,p}$). (b) BRDF ratio $D_{i,p}$.

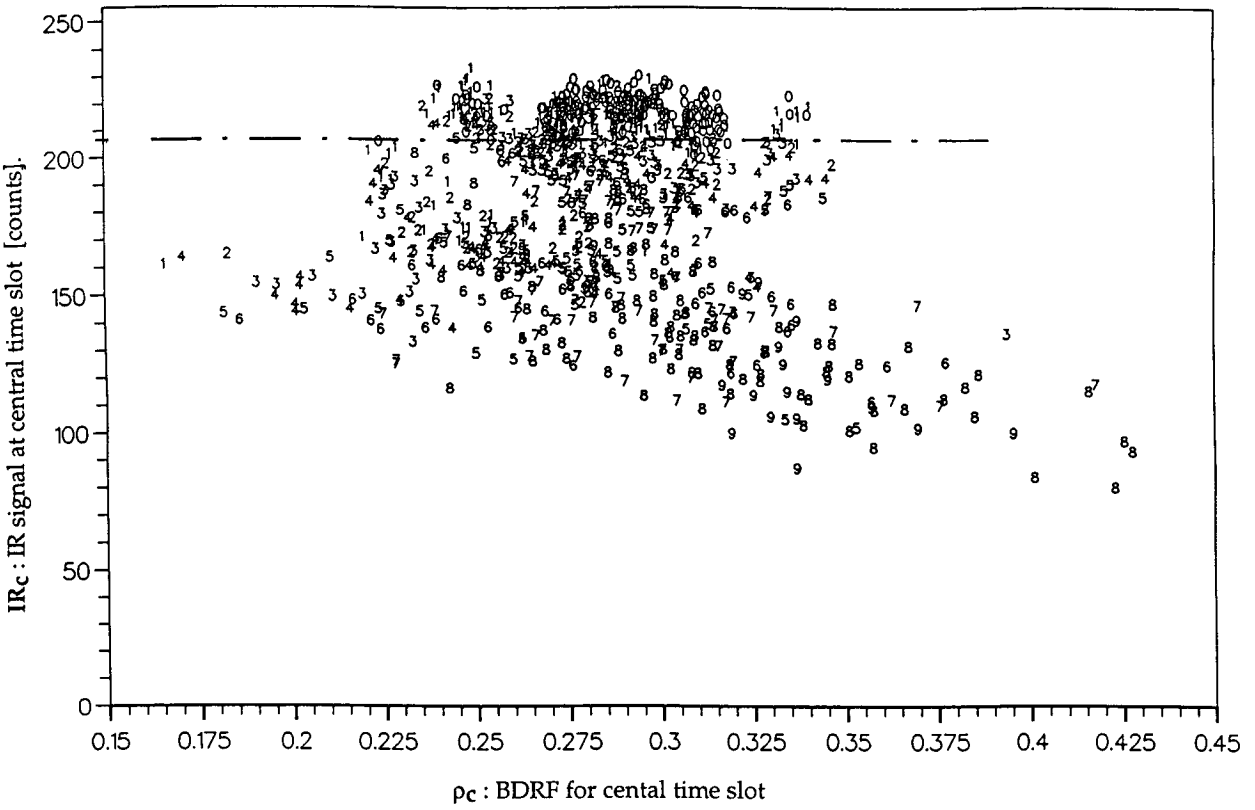

FIG. 4. The $G(\rho_c, \mathrm{IR}_c)$ graph, July 1985, Sahara and Sahel zones. Each point on graph represents one day (in this month), one area (in these zones). G: ISCCP C1 cloud cover class defined in Table 4; ρ_c: BDRF for central time slot; IR_c: IR signal at central time slot. Threshold for a boundary between clear ($G = 0$) and cloudy ($G > 0$) points is drawn.

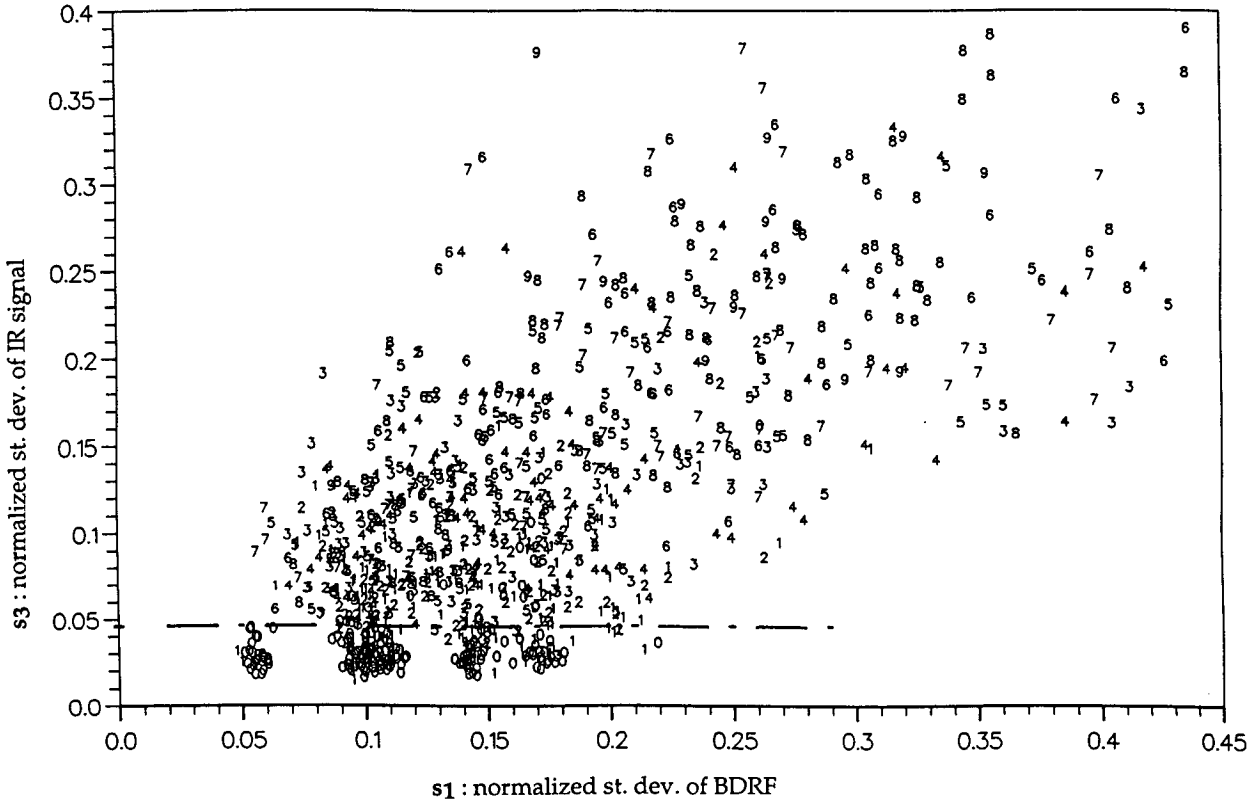

FIG. 5. Same as Fig. 4 but $G(s_1, s_3)$ graph. G: ISCCP C1 cloud cover class defined in Table 4; s_1: normalized standard deviation of BDRF at central time slot, defined by Eq. (7); s_3: normalized standard deviation of IR signal at central time slot, defined by Eq. (9). Threshold for a boundary between clear ($G = 0$) and cloudy ($G > 0$) points is drawn.

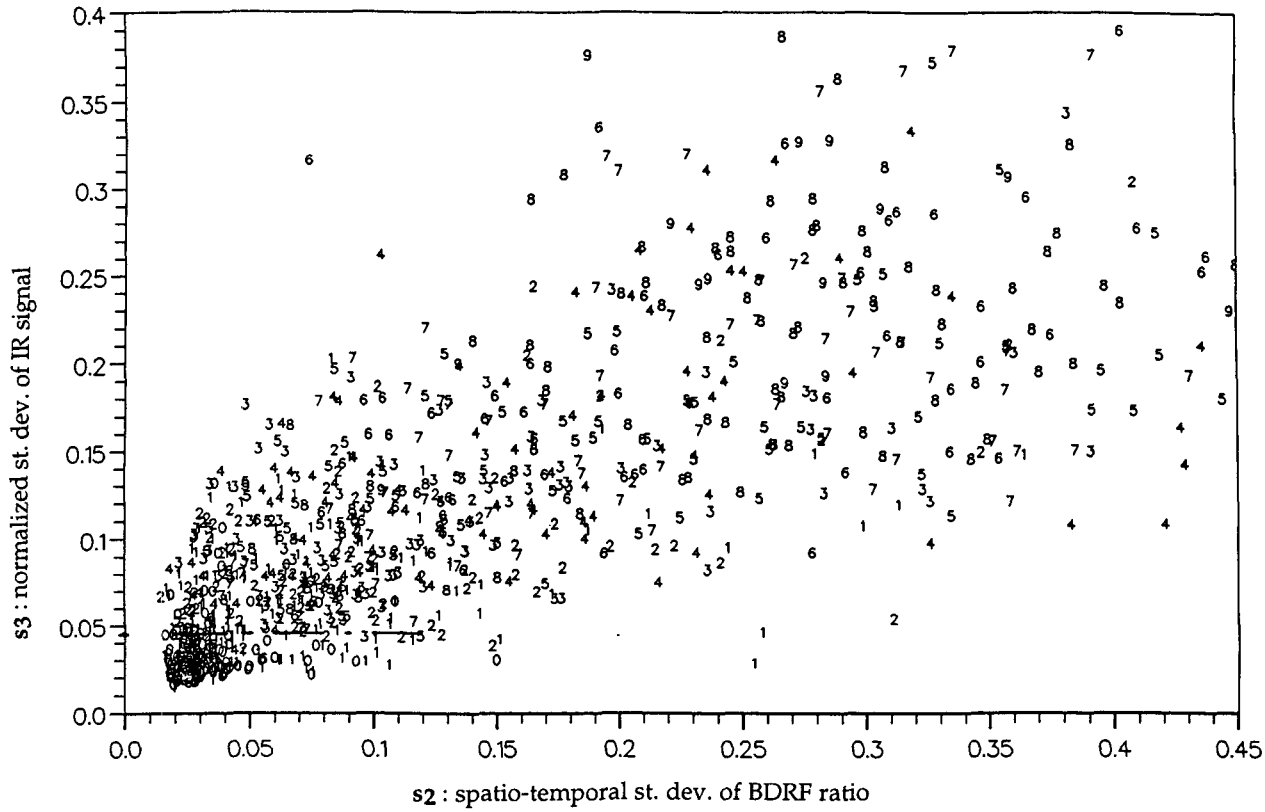

FIG. 6. Same as Fig. 4 but $G(s_2, s_3)$ graph. G: ISCCP C1 cloud cover class defined in Table 4; s_2: mean over time of spatial standard deviation of BDRF ratio, defined by Eq. (8); s_3: normalized standard deviation of IR signal at central time slot, defined by Eq. (9). Threshold for a boundary between clear ($G = 0$) and cloudy ($G > 0$) points is drawn.

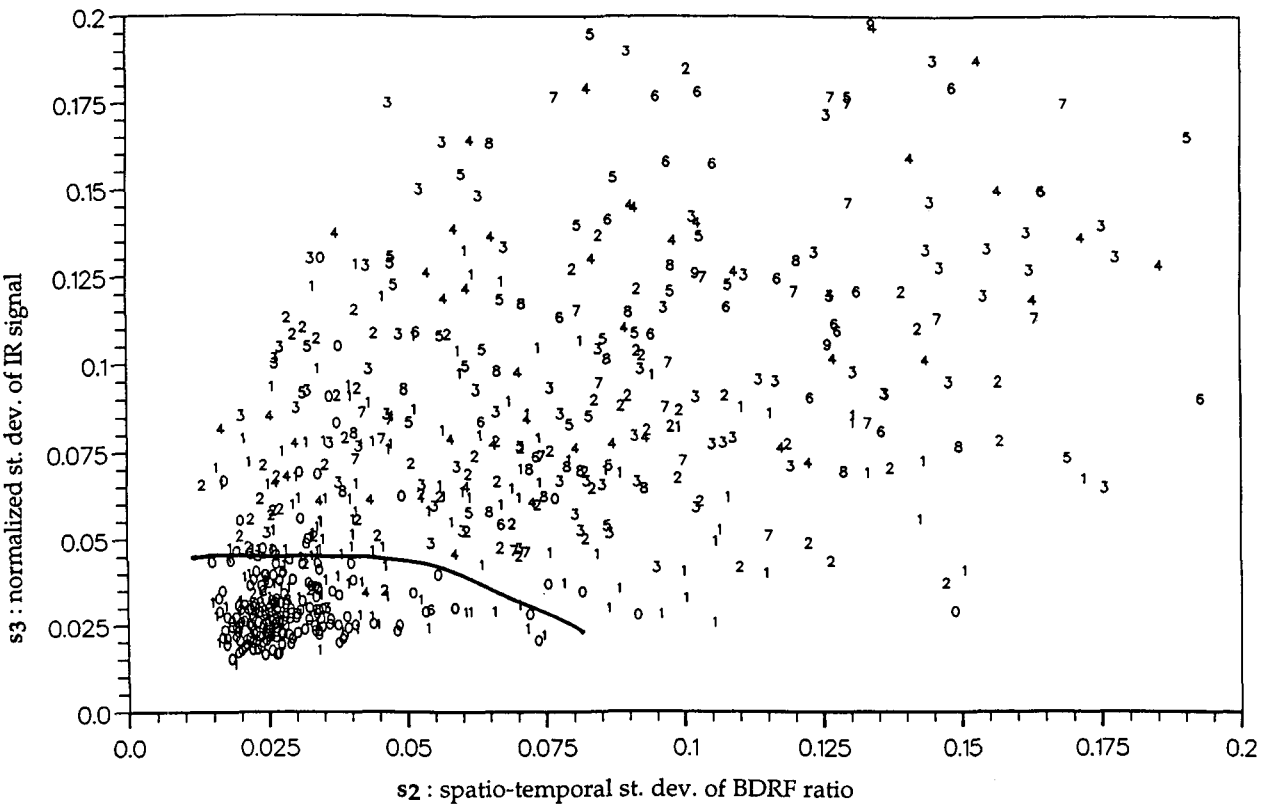

FIG. 7. The $G(s_2, s_3)$ graph. July 1985 Sahara zone. A boundary between $G = 0$ points (clear sky) and $G > 0$ points (cloudy) (note the scale dilations in regard to Figs. 4–6).

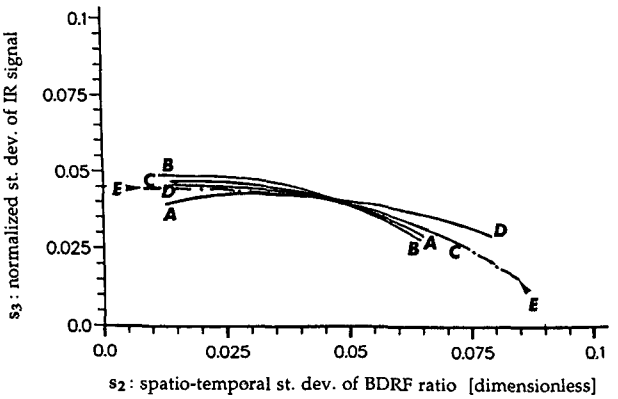

FIG. 8. Boundaries for Sahara, on $G(s_2, s_3)$ graph, for 1985 for the four seasons of 1985 (A: December, January, February; B: March, April, May; C: June, July, August; D: September, October, November; E: mean boundary for the four seasons).

possible meteorological variation and because the angles themselves vary with time. If all N points are of same type $n(p, i) = n$ (clear desert in our case), then

$$A[p, n(p, i)] = A[p, n] = A_p$$

$$\alpha[n(p, i), i] = \alpha(i)$$

$$R[n(p, i), i] = R(i)$$

and

$$\rho_i = \langle A_p \rangle \alpha(i) R(i).$$

The spatial variance of the BDRF is then

$$\sigma(\rho_i) = \alpha(i) R(i) \sigma(A_p),$$

which can be given in normalized form as, from Eq. (7):

$$s_1 = \frac{\sigma(A_p)}{\langle A_p \rangle},$$

measuring the spatial heterogeneity of cloud-free desert area. In the general case, we have

$$s_1 = \frac{\sigma(A_{pc}\alpha_{pc}R_{pc})}{\langle A_{pc}\alpha_{pc}R_{pc} \rangle},$$

where $A_{pc}\alpha_{pc}R_{pc} = A[p, n(p, c)]\alpha[n(p, c), c]R[n(p, c), c]$, which depends on the distribution of scene types $n(p, c)$ at the central time slot c, and on the corresponding angular functions.

Considering the BDRF ratio:

$$D_{i,p} = \frac{\rho_{i,p}}{\rho_{c,p}} = \frac{A_{pi}\alpha_{pi}R_{pi}}{A_{pc}\alpha_{pc}R_{pc}}$$

we note that if scene type is the same (clear desert) for all N points p, at time slots i as well as c, we have A_{pi} as a function of analysis point but not of time, that is,

$$A_{pi} = A_{pc} = A_p, \quad \text{all } i,$$

whereas $D_{i,p}$ is a function of time but not of analysis point. Thus we can write

$$D_{i,p} = \frac{\alpha(i)R(i)}{\alpha(i)R(i)} = D_i,$$

which is independent of p, so that the spatial standard deviations are equal to 0:

$$\sigma(D_{i,p}) = \sigma(D_i) = 0$$

for the different time slots i and the auxiliary variable s_2 defined by Eq. (8) as mean value of two spatial standard deviations is equal to 0:

$$s_2 = 0$$

even if A_p varies over a wide range. In the general case, however, $D_{i,p}$ varies strongly from point to point, so that s_2 takes values substantially greater than 0, even if the desert surface itself is quite homogeneous (s_1 small in the absence of clouds). It is true that a perfectly homogeneous overcast situation would yield a small value of s_2, but such a uniform distribution of cloud optical thickness is unlikely.

3. Observed distributions of BDRF ratio and spatial heterogeneity parameters

a. Example of a Saharan area

As an example, consider the detailed results of this analysis for the Tamanrasset (Hoggar, Algeria) area of

TABLE 4. Cloud cover classes following ERBE, ISCCP C1 (noted C1), and the distance criterion (noted D1) developed in this study, the last of these depending on the normalized distance defined in Eqs. (13) and (14). ERBE scene identification categories: CL (clear), PC (partly cloudy), MC (mostly cloudy), and OV (overcast); F and F^*: fractions of cloud cover. G and G^*: cloud cover classes.

ERBE	C1 fraction F	C1 class G	D1 class G^*	D1 fraction F^*	D1 distance d
	0.00			0.00	0
CL		0	0		
	0.05			0.05	1
PC		1	1		
	0.20			0.20	2
		2	2		
	0.30				
PC		3		0.35	3
	0.40				
		4	3		
	0.50			0.50	4
		5	4		
	0.60				
MC		6		0.65	5
	0.70				
		7	5		
	0.80			0.80	6
MC		8	6		
	0.95			0.95	7
OV		9	7		
	1.00			1.00	>8

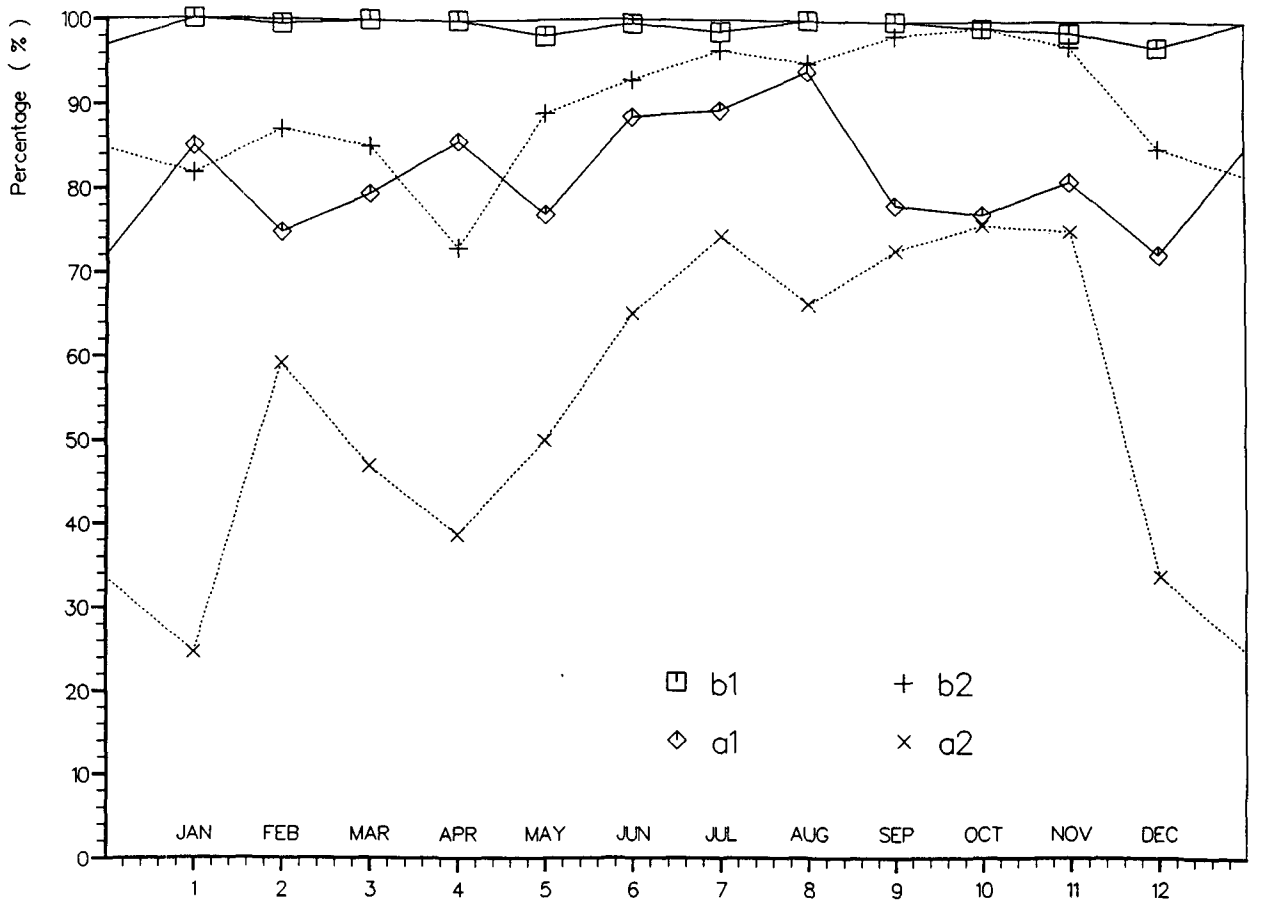

FIG. 9. Graph of a_1, a_2, b_1, and b_2 values for Sahara in 1985. N_1: total number of points $G = 0$ (clear for C1 criterion); N_2: total number of points $G^* = 0$ (clear for D1 criterion); a_1: (number of points $G^* = 0)/N_1$; b_1: (number of points $G^* = 0$ or $1)/N_1$; a_2: (number of points $G = 0)/N_2$; b_2: (number of points $G = 0$ or $1)/N_2$.

the Sahara Desert (see Table 2) for 5 July 1985. This area includes 42 analysis points p, including volcanic mountains (Hoggar), sandstone plateaus (Tassili du Hoggar, Tassili des Ajjer), and sandy regions (Erg Admer, Tenere), so that there is considerable spatial variability in the BDRF (Fig. 3a). For time slot $i = c - 1$ [0848 UTC = 0906 LST (local solar time)], the minimum value of the BDRF is 0.15, the maximum 0.32. For the entire area at central time slot, we find mean BDRF $\rho_c = 0.247$ with standard deviation $\sigma(\rho_c) = 0.041$, so that parameter $s_1 = 0.167$. On the contrary, BDRF ratio varies very little: for time slots $i = c - 1$ and $i = c + 1$, values of $D_{i,p}$ lie between 0.87 and 1.03, with most between 0.93 and 1.02. We find $D_{c-1} = 0.965$, $D_{c+1} = 0.966$, $\sigma(D_{c-1}) = 0.042$, and $\sigma(D_{c+1}) = 0.036$ so that $s_2 = 0.037$. The distribution of BDRF ratio (reflectance ratio) is much more sharply peaked than that of BDRF (apparent albedo) (Fig. 3).

b. *Distribution of ISCCP-classified data*

The ISCCP (Schiffer and Rossow 1983; Rossow et al. (1988) has produced a C1 dataset giving information on cloud cover for the whole earth. These data have a nominal spatial resolution of 30 km and temporal resolution of 3 h produced by sampling the full-resolution imaging data. Global coverage is provided by five geostationary satellites and at least one polar orbiting satellite. For the present study, all data proceed from Meteosat. The ISCCP atmosphere data are collected into a global equal-area map grid with a cell area equivalent to a 2.5° × 2.5° cell at the equator. The cells are formed by equal increments in latitude and variable longitude increments.

In particular, an ISCCP cloud cover fraction, noted F_q, can be computed as the ratio of the number of cloudy Meteosat pixels in C1 grid cell q, to the total number of pixels in that area.

We consider now the desert areas of our study, each of which overlaps 6–8 cells q of the C1 grid; each area contains N (typically 40) subareas (analysis points) p. Each cell q contains 1–12 analysis points p, and we set the cloud cover fraction for each point equal to the ISCCP C1 value for cell q, that is, $F_p = F_q$. Then the

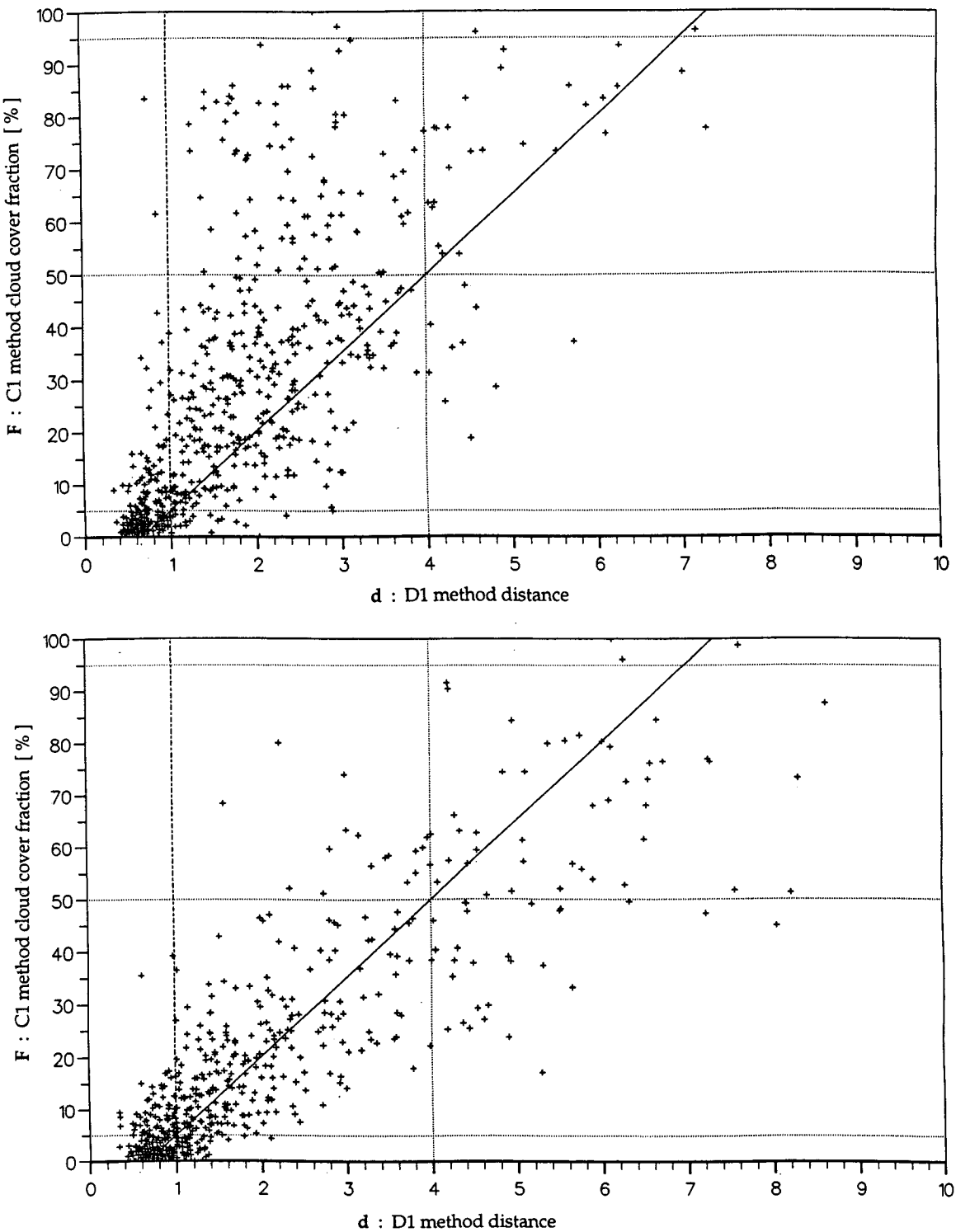

FIG. 10. Graphs of F cloud cover (%) versus distance d, in 1985, for (a) Sahara, July; (b) Sahara, October. F: ISCCP C1 cloud cover; $d = d(s_2, s_3)$: distance defined by Eq. (13).

mean value of the ISCCP cloud cover fraction for the area is

$$F = \frac{1}{N} \sum_{p=1}^{N} F_p. \qquad (12)$$

In what follows, we have defined 10 cloud cover classes (Table 4), which fit into the ERBE scene identification categories (Smith et al. 1986; Wielicki and Green 1989) clear, partly and mostly cloudy, and overcast. In Fig. 4 we show the distribution of central time slot values of mean IR signal and BDRF for the full set of Saharan and Sahelian areas (34) and all days of July 1985, with identification of the cloud cover class G corresponding to the value of F from Eq. (12). This graph is noted $G(\rho_c, \mathrm{IR}_c)$.

Although many different cloud cover detection and analysis algorithms exist (cf. Rossow et al. 1989; Rossow 1989), for most of these the daytime algorithm uses a combination of visible and infrared thresholds, based on the principles that clouds are brighter in the visible than the underlying surface (except snow); and clouds (especially high clouds) are generally colder than the underlying surface, so that the infrared signal should be lower.

In our study, the use of BDRF ratio and its variability in space and time allows us to sharpen these criteria. We note that in Fig. 4, which corresponds to the "classical" method, the values of BDRF exhibit considerable scatter and do not provide a useful threshold to dis-

TABLE 5. Coordinates, in the s_3–R_{IR} plane, of the 10 points delimiting the seven parts in Fig. 11; s_3: normalized standard deviation of IR signal defined by Eq. (9); R_{IR}: IR ratio defined by Eq. (15).

R_i	s_3	R_{IR}	Notes
R_0	0.000	0.900	Eq. (16)
R_1	0.045	0.920	Eq. (16)
R_2	0.045	0.900	Eq. (17)
R_3	0.500	0.000	Eq. (17)
R_4	0.140	0.719	
R_5	0.230	0.719	
R_6	0.800	0.210	
R_7	0.230	0.548	
R_8	0.350	0.548	
R_9	0.350	0.320	

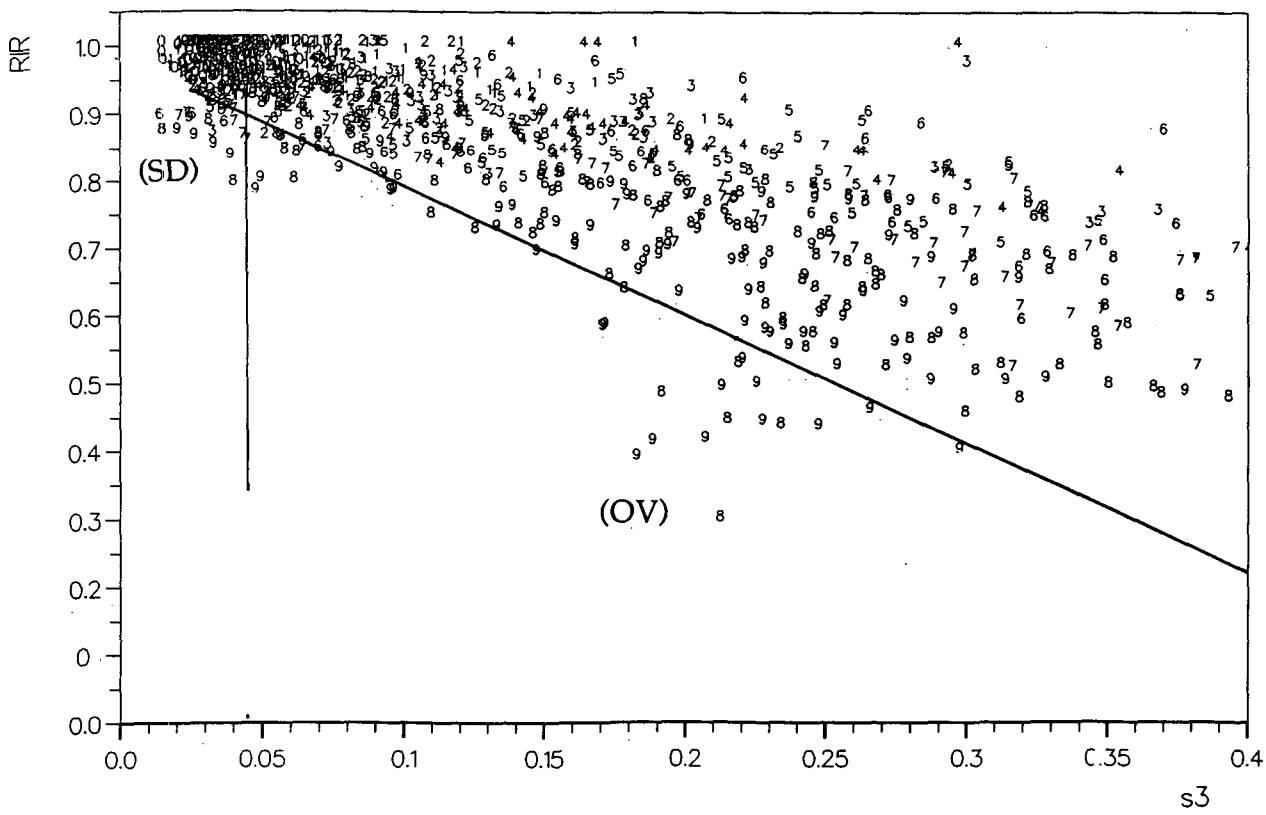

FIG. 11. The $G(s_3, R_{IR})$ graph for Sahara and Sahel, March 1985. General view for detection of overcast (OV) and Saharan dust (SD) events. G: ISCCP C1 cloud cover class defined in Table 4; s_3: normalized standard deviation of IR signal defined by Eq. (9); R_{IR}: IR ratio defined by Eq. (15). Points below solid line are defined as "overcast" (OV) or "Saharan dust" (SD), respectively, parts W, X or parts Y, Z in Fig. 12.

criminate cloudy and clear areas. A fairly well defined infrared threshold does exist, but it varies strongly with season. For example, for Sahara, we obtain the following thresholds (in IR count units): January: 150, April: 200, July: 205, October: 180.

We can, however, use the quantities defined in Eqs. (7)–(9) above. Considering the relative spatial variabilities of BDRF and IR signal, we plot the distribution of $G(s_1, s_3)$ in Fig. 5. In this case the IR threshold ($s_3 \approx 0.05$) is independent of season.

Some tendency of clustering is observed in ρ_c (Fig. 4) and s_1 (Fig. 5); we see four clusters with significantly different values, corresponding to four different surface types according to different BDRF in the Saharan–Sahelian zone. For example, in $G(s_1, s_3)$ graph, the cluster centered on $s_1 = 0.055$ and $s_3 = 0.025$ results only from area 15 (Sabha, central Sahara).

A much simpler clustering of clear-sky values ($G = 0$) appears when we replace s_1 by s_2, that is, considering the relative spatial and temporal variability of the BDRF ratio. This appears clearly in Fig. 6 where we plot the distribution of $G(s_2, s_3)$. For each distribution of $G(s_2, s_3)$, the graph contains N_0 points, depending on the number of areas in the zone and the number of days in the month, diminished by the number of missing data points. For example, in July 1985 for the Saharan zone, $N_0 = 679$. Of these points, N_1 correspond to $G = 0$, that is, to cloud-free areas according to the ISCCP C1 classification. We seek to separate the s_2–s_3 plane into two domains, one of which contains 85% of the N_1 points for which $G = 0$. Figure 7 illustrates the drawing of such a boundary for the Saharan zone in July 1985.

TABLE 6. Relationship between s_3–R_{IR} graph parts and F^* values: s_3 and R_{IR} are IR related values defined by Eqs. (9) and (15); F^*: cloud cover with distance d method; $d = d(s_2, s_3)$: distance defined by Eq. (13).

Parts	F^*
A	$-0.10 + 0.15d$
U	0.84
V	0.95
W	0.99
X	0.88
Y	0.35
Z	0.74

c. *Distributions of $G(s_2, s_3)$*

For each of the four arid zones considered (Sahara, Sahel, Arabia, Namib–Kalahari), and for each

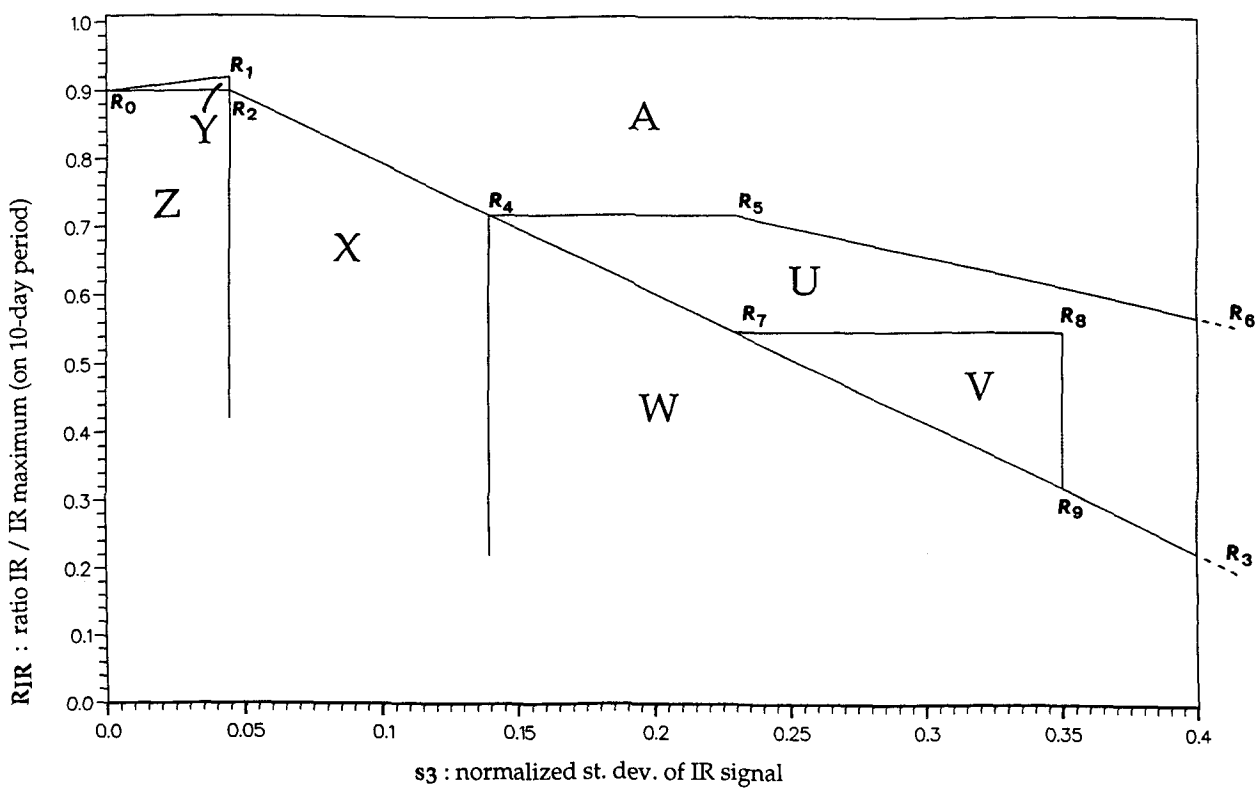

FIG. 12. The seven parts in a s_3–R_{IR} graph created after systematic study of $G(s_3, R_{IR})$ graphs, for the four zones and the 12 months in 1985. Part A (about 90% of available data): linearity between cloud cover and distance $d(s_2, s_3)$. Parts U, V, W, X (about 8% of available data): cloud cover large. Parts Y and Z (about 2% of available data): Saharan dust events.

TABLE 7. Occurrence frequency of each event for each area in 1985. 0: no data available. A: general case. U to X: mostly cloudy to overcast events. Y, Z: Saharan dust events.

No.	0	A	U	V	W	X	Y	Z	Total
Sahara									
01	18	289	14	7	9	12	9	7	365
02	18	299	10	7	4	10	8	9	365
03	18	290	21	5	9	5	3	14	365
04	18	303	15	1	6	3	5	14	365
05	18	301	25	3	4	10	3	1	365
06	18	319	8	1	5	3	5	6	365
07	18	301	15	5	2	11	4	9	365
08	18	307	18	8	2	6	2	4	365
09	18	312	17	4	7	4	3	0	365
10	18	333	7	1	0	2	2	2	365
11	18	314	22	3	3	3	1	1	365
12	18	313	17	4	5	6	1	1	365
13	19	329	4	0	0	5	4	4	365
14	19	311	11	3	3	5	8	5	365
15	19	301	16	4	5	11	5	4	365
16	18	337	5	1	1	1	0	2	365
17	18	322	14	1	0	6	3	1	365
18	18	327	8	0	0	4	5	3	365
19	22	314	8	3	4	5	5	4	365
20	22	310	2	0	2	7	11	11	365
21	25	323	1	0	0	2	8	6	365
22	25	308	9	1	6	6	6	4	365
Total	421	6863	267	62	77	127	101	112	8030
Total percentage	5	85	3	1	1	2	1	1	100
Sahel									
23	18	296	30	5	7	5	1	3	365
24	18	307	30	0	4	2	1	3	365
25	18	307	22	2	4	6	2	4	365
26	18	312	19	2	2	8	0	4	365
27	18	319	14	2	0	7	2	3	365
28	18	316	12	0	1	13	4	1	365
29	18	307	14	0	5	16	3	2	365
30	18	325	19	0	1	2	0	0	365
31	18	333	9	1	1	2	1	0	365
32	22	306	13	1	1	14	1	7	365
33	25	306	21	1	1	3	3	5	365
34	25	318	5	1	2	9	2	3	365
Total	234	3752	208	15	29	87	20	35	4380
Total percentage	5	86	5	0	1	2	0	1	100
Arabian Desert									
35	33	292	11	3	3	7	4	12	365
36	33	304	4	2	1	6	4	11	365
37	33	294	15	3	6	11	1	2	365
38	31	305	22	1	4	1	1	0	365
39	30	289	20	1	11	10	2	2	365
Total	160	1484	72	10	25	35	12	27	1825
Total percentage	9	81	4	1	1	2	1	1	100
Namib Kalahari									
40	18	299	32	1	4	8	1	2	365
41	18	293	27	2	8	11	4	2	365
42	18	320	16	2	2	3	2	2	365
Total	54	912	75	5	14	22	7	6	1095
Total percentage	5	83	7	0	1	2	1	1	100
Total	869	13 011	622	92	145	271	140	180	15 330
Total percentage	6	85	4	1	1	2	1	1	100
Percentage of available data	—	90	4	1	1	2	1	1	100

month—January to December of 1985, January for years 1984–86, July for years 1983–86—we plot the distribution of $G(s_2, s_3)$.

To examine possible seasonal variations of the domain boundary, we consider (Fig. 8), for each of our four arid zones, the boundaries we can draw for the four seasons of 1985 (A: December, January, February; B: March, April, May; C: June, July, August; D: September, October, November) as well as for the mean value over the year. We also consider interannual changes of the boundaries for July, and find them to be small. For each of the four zones, the boundaries are independent of the month; the four seasonal mean curves have the same appearance and surround the annual mean curve; the annual mean boundaries are essentially the same for the four zones.

d. Distinguishing clear and cloudy scenes using s_2 and s_3

We conclude that clear and cloudy scenes can be discriminated over each of the desert zones using a single boundary criterion, independent of the desert zone and the month. The elliptical boundary can be

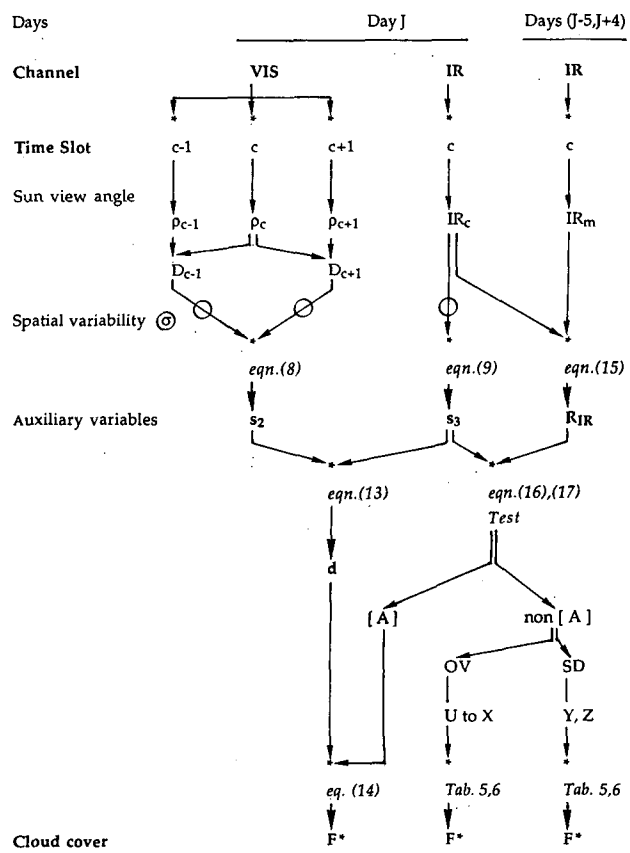

FIG. 13. Diagram of the method to obtain F^* value from VIS and IR data with the notations used above.

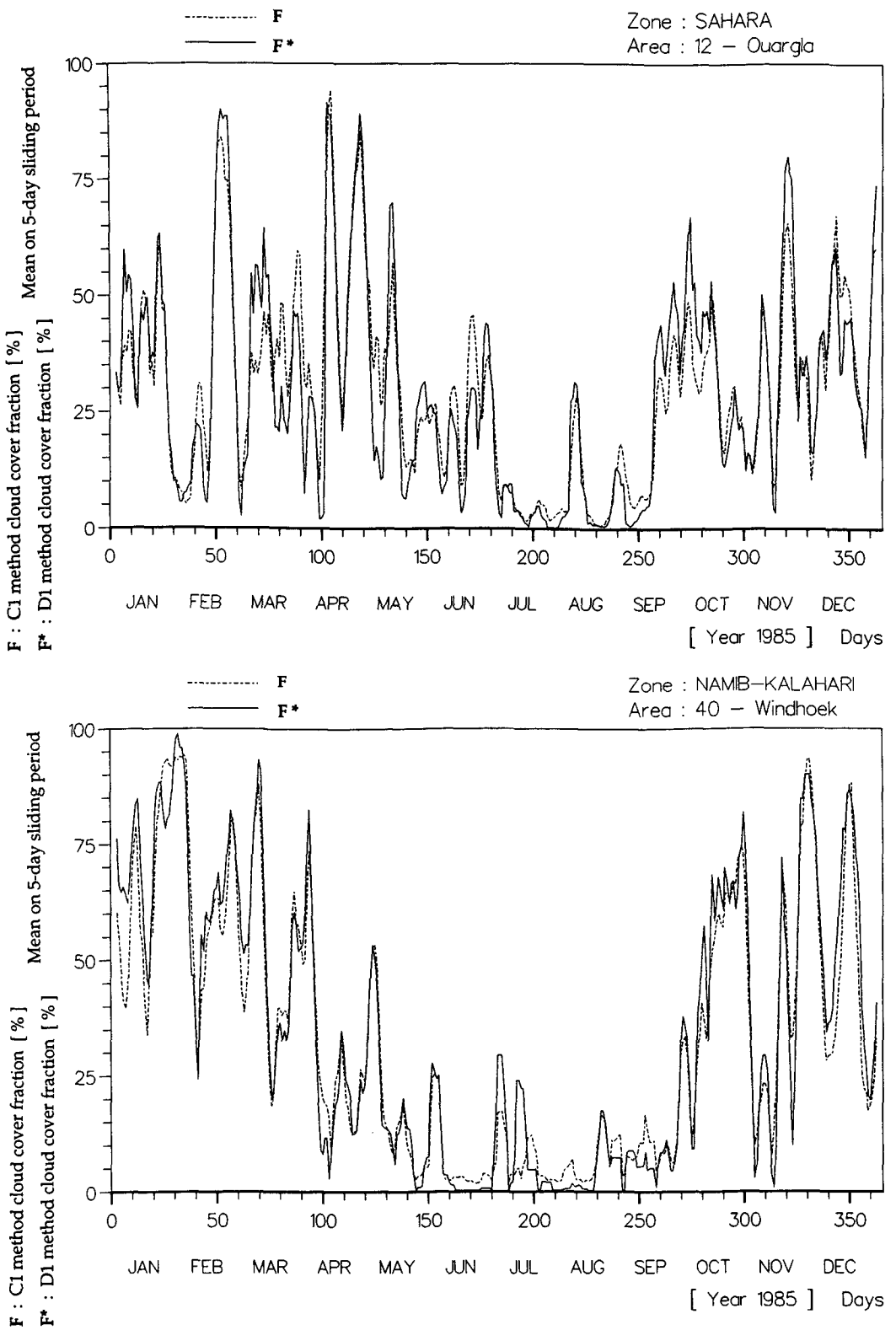

FIG. 14. Comparison between F and F^* cloud cover (%), during the year 1985, for the mean on sliding 5-day period. (a) Area 12 (Ouargla), Sahara zone. (b) Area 40 (Windhoek), Namib–Kalahari zone. F: C1 criterion cloud cover; F^*: D1 criterion cloud cover.

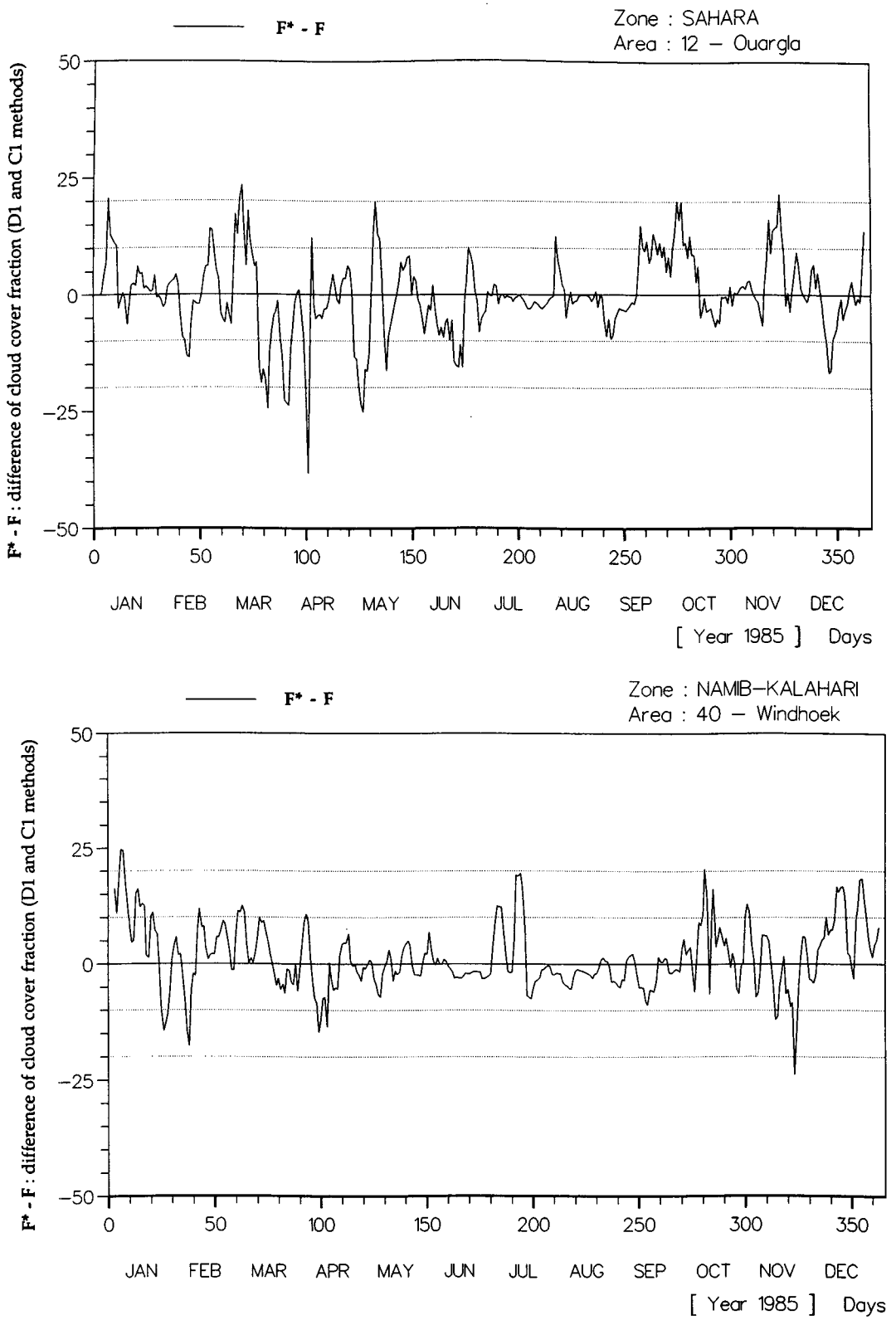

FIG. 15. Difference $F^* - F$ graph during 1985, for the mean on sliding 5-day period, for the same locations as in Fig. 14.

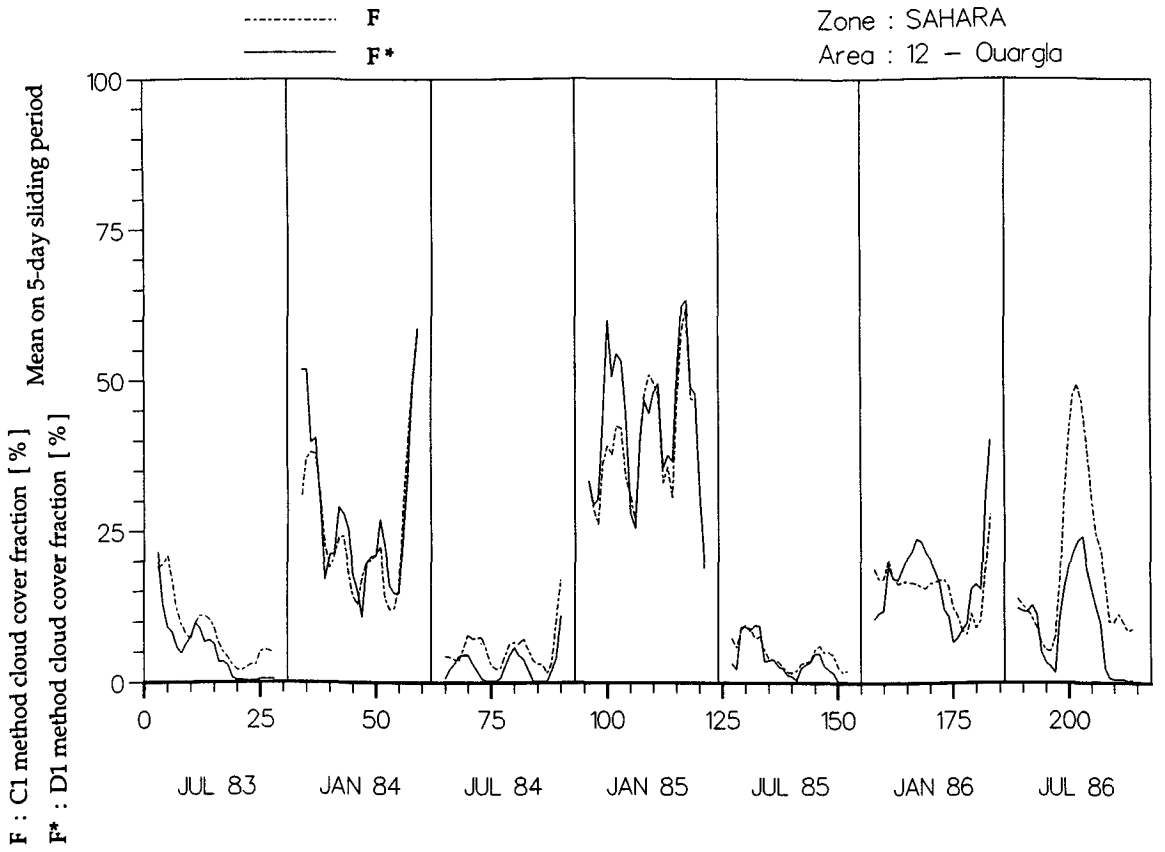

FIG. 16. Comparison between F and F^* cloud cover (%), during the months January and July, from July 1983 to July 1986, for the mean on sliding 5-day period. Area 12 (Ouargla), Sahara zone.

chosen, with semimajor axis $s_{2o} = 0.090$ on the s_2 axis (heterogeneity of the BDRF ratio) and semiminor axis $s_{3o} = 0.045$ on the s_3 axis (normalized IR heterogeneity). Defining a normalized distance d in the s_2–s_3 plane as:

$$d = d(s_2, s_3) = \left[\left(\frac{s_2}{s_{2o}}\right)^2 + \left(\frac{s_3}{s_{3o}}\right)^2\right]^{1/2}, \quad (13)$$

we consider that the scene is clear (i.e., cloud cover is less than 5%) if $d \leq 1$. This clear-sky criterion signifies that 85% of the points classified as clear by ISCCP C1 ($G = 0$) are inside the ellipse.

We note that the ellipse boundary is easily defined at all seasons for the Saharan and Namib–Kalahari Desert zones. For the Sahelian zone, the boundary cannot be determined during the rainy season (May–October) because of the lack of points classified as clear ($G = 0$). For the Arabian Desert zone, accuracy is poor in the winter, because the sun has set at time slot $i = 5$ and only time slot $i = c - 1 = 3$ can be used to calculate s_2 [Eq. (8)].

Notwithstanding these difficulties, for every point in the s_2–s_3 plane we compute a normalized distance d, and we attribute to it a "distance class" G^* defined in Table 4. The results obtained by this "distance" are noted with an asterisk as results of the D1 method. Examining the results, we note that areas classified as clear by the criterion $d \leq 1$ ($G^* = 0$) belong principally to the class $G = 0$, that is, are also classified as clear by ISCCP C1; there are a few areas for which $G = 1$, but practically none with higher C1 cloud cover; areas classified as clear by ISCCP C1, that is, for which $G = 0$, are practically all in class $G^* = 0$, that is, $d \leq 1$. We compare the two methods in more detail in the following section.

4. Comparison of the D1 and ISCCP C1 results

a. Clear-sky criteria

For a given zone and month, we consider the s_2–s_3 diagram. We note that the set of N_1 points classified as clear by ISCCP ($G = 0$) corresponds fairly well although not perfectly to the set of N_2 points classified as clear ($G^* = 0$) according to our normalized distance criterion, that is, lying inside the ellipse $d = 1$. In the first set, a fraction a_1 of the points lies inside the ellipse ($d \leq 1$, $G^* = 0$); a fraction b_1 lies inside the ellipse corresponding to $d = 2$ ($G^* = 0$ or 1); we note that

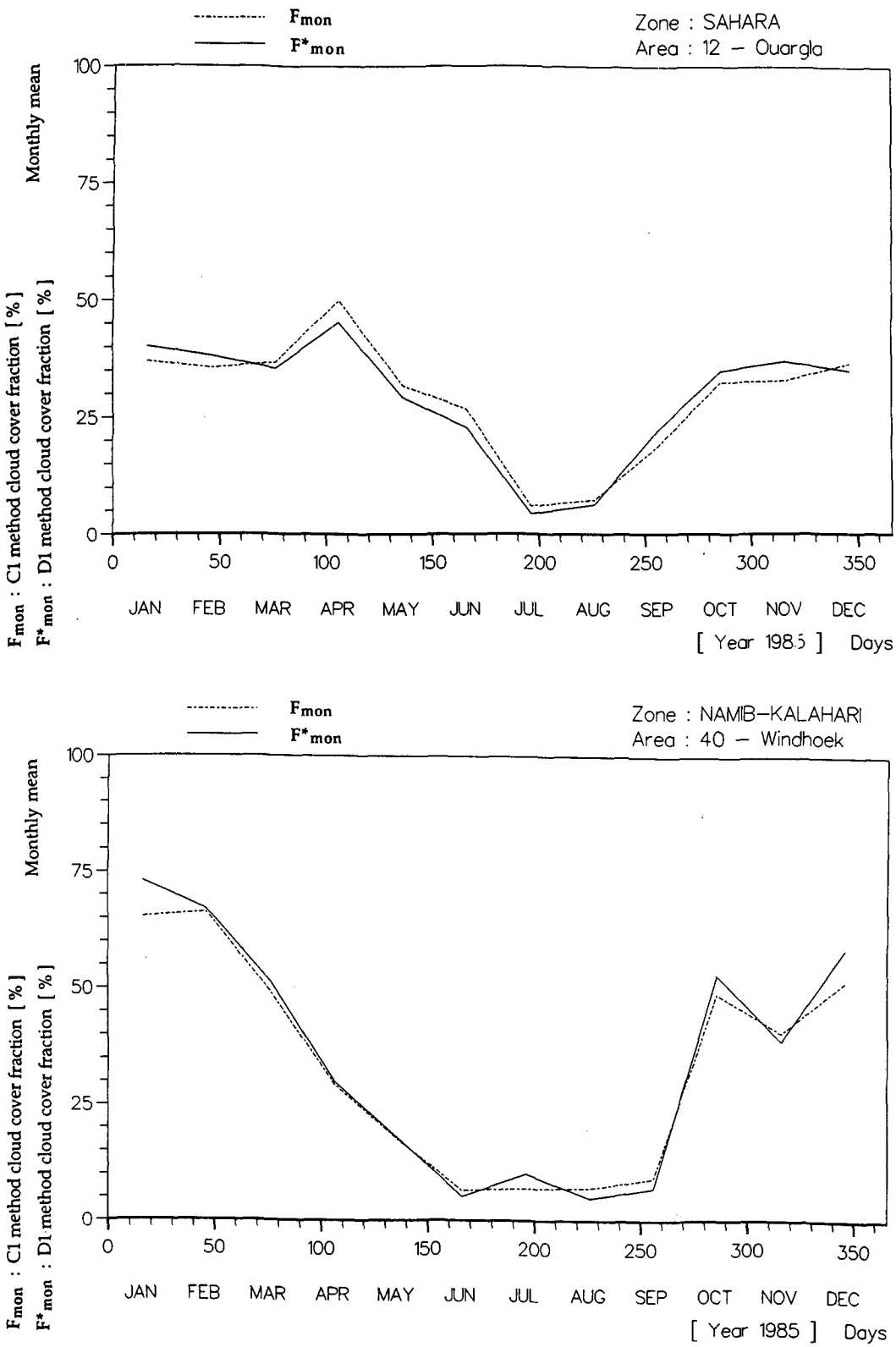

FIG. 17. Comparison between F^*_{mon} and F_{mon} cloud cover (%), during 1985, for the mean on monthly period, for the same locations as in Fig. 14.

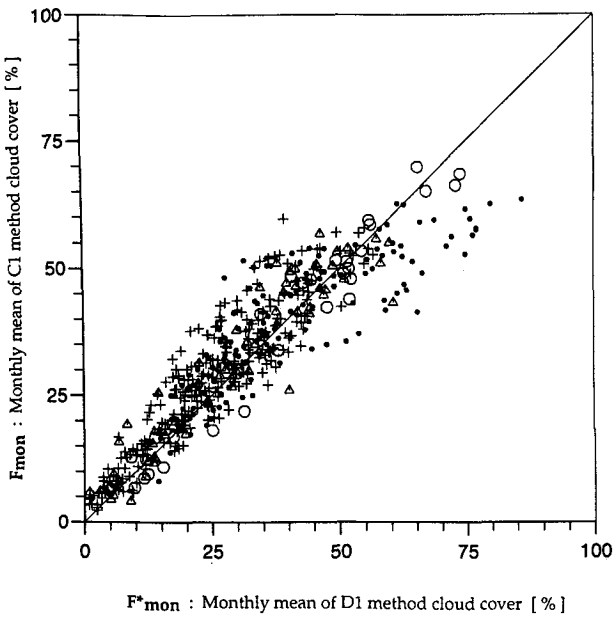

FIG. 18. Correlation between F^*_{mon} and F_{mon} (monthly values of F^* and F), for each month in the year 1985, for each area (correlation coefficient: 0.88). The zone (as defined in Fig. 1) to which each area belongs is indicated by the different symbols: for the true desert zones: +—Sahara, Δ—Arabian, ○—Namib-Kalahari; for the nontrue desert zone: ●—Sahel.

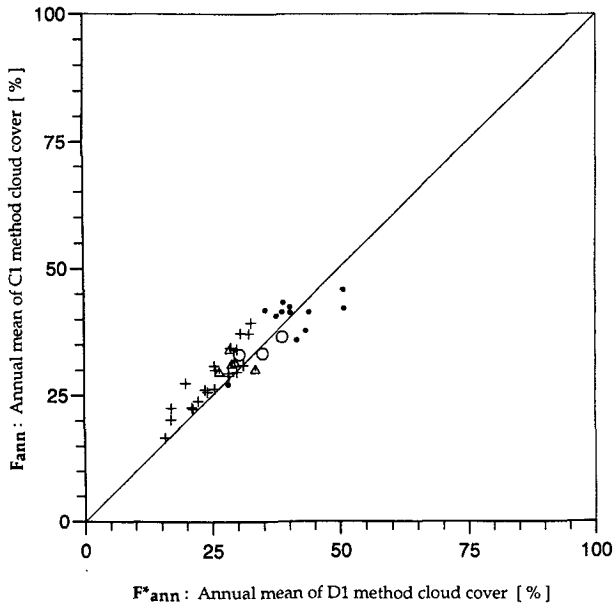

FIG. 20. Correlation between 1985 annual mean values F^*_{ann} and F_{ann}, for each area (correlation coefficient: 0.97). Symbols as in Fig. 18.

this fraction is always very close to 1. The ellipse (d = 1) was originally defined (Fig. 8) so that a_1 should equal 0.85 for a given season, but the use of a "mean" ellipse for the year leads to slight departures for this value. In the second set, that is, the set of points inside the ellipse d = 1, the fraction of points classified as clear by ISCCP (G = 0) is a_2; the fraction of points for which ISCCP gives an estimated cloud fraction less than 0.2 (G = 0 or 1) is b_2. To the extent that the

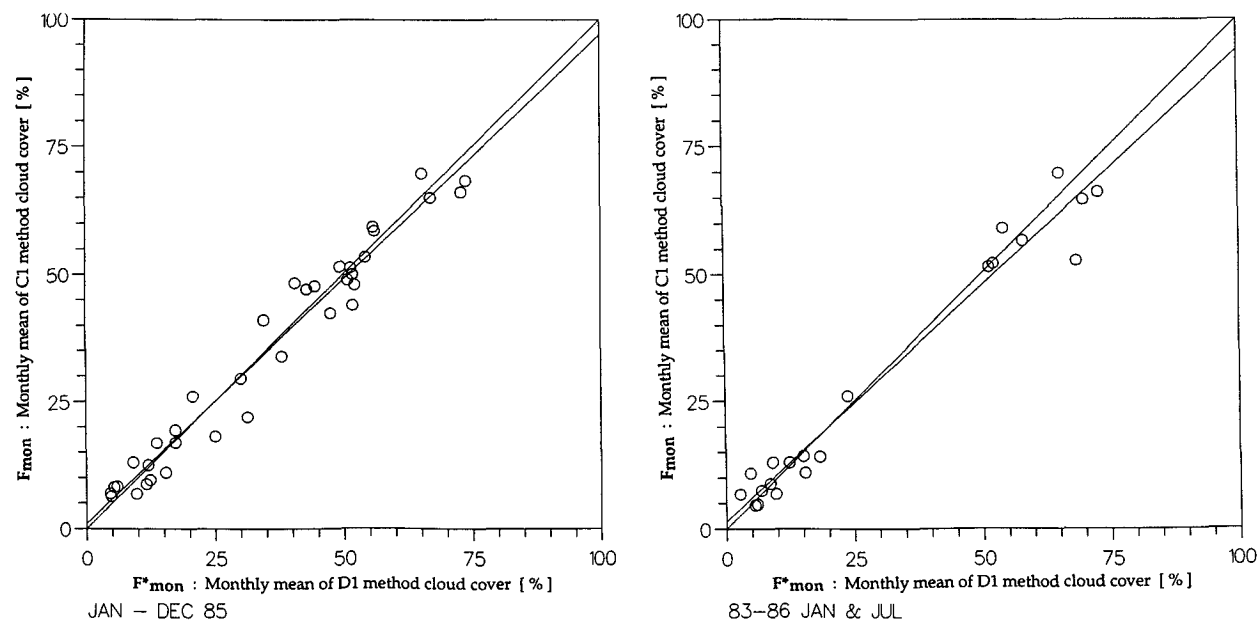

FIG. 19. Correlation between F^*_{mon} and F_{mon} (monthly values of F^* and F), for each area of Namib-Kalahari zone, noted by circle. (a) For the 12 months in 1985 (correlation coefficient: 0.85); (b) for January and July from July 1983 to July 1986 (correlation coefficient: 0.77).

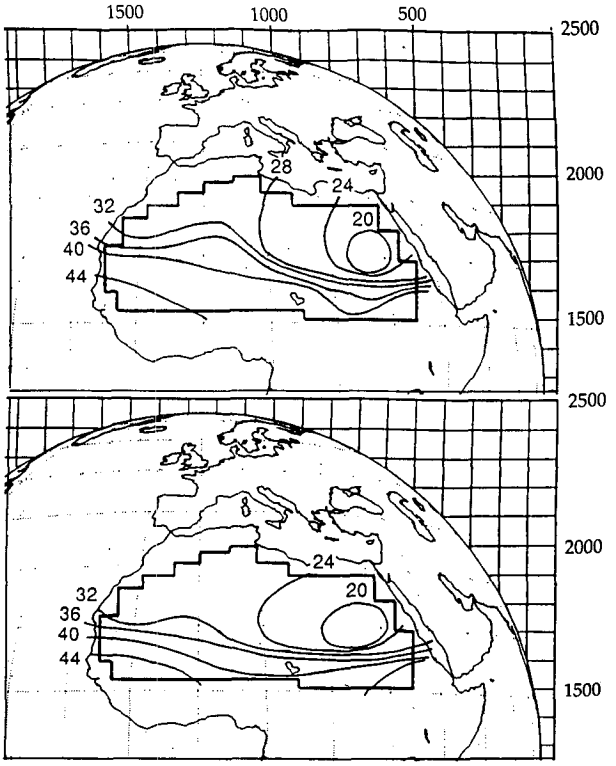

FIG. 21. Maps of Sahara and Sahel. (a) isolines of F_{ann} values (annual mean over 1985 for F, C1 criterion cloud cover); (b) isolines of F^*_{ann} values (annual mean over 1985 for F^*, D1 criterion cloud cover).

value of b_2 is close to 1, the distance criterion yields points of zero or low cloud cover.

Considering the case of the Saharan zone in July 1985, for which there are a great many clear-sky days ($N_1 = 203$, $N_2 = 246$), we find: $a_1 = 0.892$ and $b_1 = 0.985$, $a_2 = 0.736$, and $b_2 = 0.955$.

There is thus good agreement between the two methods, although the lower value of fraction a_2 shows that there is some contamination of scenes classified as clear according to the distance criterion by scenes with slight partial cloud cover (5%–20%) according to ISCCP. For comparison we consider also the case of the Namib–Kalahari zone in October 1985, for which the number of clear-sky days is small ($N_1 = N_2 = 9$). Here we find $a_1 = a_2 = 0.9$, and $b_1 = b_2 = 1.0$.

We consider all four zones and all 12 months in 1985 (Fig. 9). For the Saharan zone, fraction a_1 is practically constant at about 0.82, which is consistent with the construction of the boundary to yields 0.85. Values of b_1 are practically equal to 100%: one is certain (at 99.7%) to find ISCCP C1 clear-sky days inside the ellipse for which $d = 2$ ($G^* = 0$ or 1). Fraction a_2, which tells us what proportion of the points inside the ellipse (i.e., classified as clear according to our distance criterion) is also classified as clear by ISCCP C1, is relatively constant near 70% from June to November, but falls to 37% between December and May. Thus, a significant fraction of the points inside the ellipse corresponds to nonzero cloud cover (mostly class $G = 1$) according to ISCCP. Values of b_2 are fairly high, and remain in the range 95% (±5%) from May to November.

For the Namib–Kalahari zone, the number of clear-sky points is large only during the April–September period. Values of a_1, b_1, and b_2 are above 95%, $a_2 = 74\%$, so that there is very good correspondence between the clear-sky sets defined by the two methods.

For the Arabian Desert and Sahelian zones, we also find clear skies are also not as frequent as in the Sahara, but the b_1 values are also close to 100%. For fraction a_1 we find: for Arabian Desert, around 75% from July to October, around 50% for the rest of the year; for Sahel, no point available from June to September, around 60% for the rest of the year.

We conclude that if the overall proportion of clear-sky scenes is sufficiently large, there is a very close relation between ISCCP clear-sky scenes ($G = 0$) and scenes classified as clear according to our distance criterion ($G^* = 0$): over 80% of ISCCP C1 clear-sky days (class $G = 0$) are detected by criterion $d \leq 1$ ($G^* = 0$), and 100% by criterion $d \leq 2$ ($G^* = 0$ and 1); about 70% of scenes for which $d \leq 1$ (class $G^* = 0$) are ISCCP C1 clear-sky days ($G = 0$); 96% of these scenes are in ISCCP C1 classes $G = 0$ and 1.

b. *Estimating cloud cover from the (s_2, s_3) distance*

The success of the ($d \leq 1$) criterion in detecting clear scenes leads us to consider using the value of d to estimate cloud cover. Plotting F versus d for each month and each zone gives a more or less scattered aggregate of points for which we can derive a linear regression (Fig. 10). We find correlation coefficients around 0.8 and, if the "clear" cluster ($G = 0$ and $G^* = 0$) is omitted, around 0.9. The regression coefficients are independent of the zone and very slightly dependent on the month. The scatter is smaller for the cooler months, but the slope remains practically the same. Large (≥ 0.80) values of the ISCCP cloud cover do not appear well correlated with $d(s_2, s_3)$ in some cases (notably the Saharan zone in July 1985, Fig. 10a). The regression results lead us to propose a formula to compute cloud cover F^* from normalized distance d:

$$F^* = \begin{cases} -0.10 + 0.15d, & 0.67 < d < 7.33 \\ 0, & d < 0.67 \\ 1, & d > 7.33. \end{cases} \quad (14)$$

The results are shown in Table 4.

Note that the different graphs of $G(s_2, s_3)$ show (see Fig. 6) a very great accumulation of points 0 ($G = 0$) around the point of coordinates ($s_2 = 0.025$; $s_3 = 0.025$), corresponding to $d = 0.62$, according to Eq. (13). This is very close to $d = 0.67$ found with Eq.

(14) when $F^* = 0$. Those different graphs show also the minimum value for d as $d = 0.40$. In conclusion, we see that the C1 and D1 clear classes, $G = 0$ and $G^* = 0$, respectively, correspond to $0.40 \leq d \leq 1.00$. If $d \leq 0.67$, we take $F^* = 0$, to exclude negative values.

c. *Saharan dust clouds and homogeneous overcast scenes*

The F^* cloud cover determination assumes a linear relationship between distance d and cloud cover fraction, and thus depends on increasing heterogeneity of the scene in the visible and infrared with increasing cloud cover. This relation is at fault in two cases, desert dust clouds and total cloud cover (overcast scenes), for which heterogeneity decreases as cloud cover increases.

1) SAHARAN DUST CLOUDS

When temperatures in desert zones are very high, the phenomenon of desert (Saharan) dust clouds may occur (called "harmattan" in western Africa): over large areas (several hundred kilometers on a side), great quantities of dust are raised and set in motion (D'Almeida 1986). In 1985 there were two significant Saharan dust events (Legrand et al. 1989; Vovor 1991): from 14 to 20 February 1985 in the Sahel, and from 29 to 31 March 1985 in the western Sahara. During a Saharan dust event, the sky is mostly cloudy or overcast, but the dust clouds appear extremely homogeneous on satellite VIS and IR imagery. Values of s_2 and s_3 are small and the distance d is less than 1 (generally between 0.7 and 1.0). As a result, our method identifies such scenes as "clear" (while ISCCP identifies dust clouds as cloud); a corrective procedure is advisable.

For land scenes, areas of Saharan dust cannot be distinguished from the surrounding ground with VIS channel, and for good reason: the dust clouds are made up by the particles that make up the soils. On the contrary, with the IR channel at the central slot, these dust clouds appear a little colder than the surrounding ground (the ground is very warm at this time), but with little heterogeneity. Thus Saharan dust can be detected over land by using the IR value and its variability. Over the ocean, the presence of Saharan dust is obvious on VIS images, and just barely detectable on IR images. Over dust clouds lasting for periods of a few days, the IR value remains practically constant for a given area at a fixed time (central time slot c), provided that the area remains free of other (water/ice) clouds. Decrease of the value of IR_c relative to a maximum value (to be defined) indicates cloud contamination.

To study the problem, we have considered sliding periods of 10 days over each area, and extracted the maximum values IR_m of IR_c over these periods. With 10 days we are sure of finding at least one clear-sky day over each desert area, without needing to take seasonal variation into account. We define the ratio

$$R_{\mathrm{IR}} = \frac{\mathrm{IR}_c}{\mathrm{IR}_m}, \tag{15}$$

which is equal to 1 if the scene is clear, and decreases as cloud cover increases. We plot R_{IR} against s_3 and identifying points according to G (Fig. 11). On this $G(s_3, R_{\mathrm{IR}})$ graph, cases of desert dust stand out as having values of R_{IR} that are anomalously low (but still above 0.7), for very low values of s_3. Study of several Saharan dust events lead us to set the threshold of s_3 at 0.045 and that of R_{IR} in the range 0.90–0.92. We write the criterion for Saharan dust as

$$s_3 \leq s_{3o} \quad (\text{with } s_{3o} = 0.045)$$

$$R_{\mathrm{IR}} \leq 0.90 + 0.02\left(\frac{s_3}{s_{3o}}\right). \tag{16}$$

This criterion detects all Saharan dust events found by Vovor (1991) for the year 1985.

2) OVERCAST SCENES

The case of complete cloud cover, quite rare in desert zones, gives effects that are analogous to Saharan dust, with a scene that is homogeneous, although less so, than a dust cloud scene. In such cases the decrease of the IR signal is pronounced, and R_{IR} varies between 0.6 and 0.3, falling to 0.2 in some cases. The ratio s_3/s_{3o} is found to lie in the range 3.5–5.5, which usually corresponds to cloud cover of order 40%–60%, whereas in this case cloud cover is total (95%–100%). Figure 11 shows that these cases form a distinct group, and we can write the criterion for homogeneous overcast scenes as

$$s_3 > s_{3o}$$

$$R_{\mathrm{IR}} \leq 0.90 - 1.9014(s_3 - s_{3o}). \tag{17}$$

3) SURVEY OF DUST CLOUDS AND OVERCAST SCENES

On Fig. 11, representing the $G(s_3, R_{\mathrm{IR}})$ graph for the full set of Saharan and Sahelian areas and all days of March 1985, the two phenomena, dust clouds and overcast scenes, appear very distinctly.

A systematic study of $G(s_3, R_{\mathrm{IR}})$ graphs for all zones, all months in year 1985, and other months (January and July for the years noted above) yields criteria for important cloud cover ($G = 8$ and 9) and dust clouds.

This study leads us to divide the s_3–R_{IR} graphs into seven parts. On this diagram (Fig. 12), these seven parts are delimited by 10 points, called R_0 to R_9 (Table 5). These seven parts are:

Part A (about 90% of available data): linearity between cloud cover F^* and distance $d(s_2, s_3)$. The G

classes vary between 0 and 7, and the cloud cover F between 0.00 and 0.80.

Parts U, V, W, X (about 8% of available data), large cloud cover:

U ($G = 8$), with F mean: 0.84;
V mainly ($G = 9$), with F mean: 0.95;
W very homogeneous cloud cover (s_3 smaller than in V), only overcast scenes, with F mean: 0.99;
X difficult to classify, includes classes ($G = 7$, 8 and 9), with F mean: 0.88;

Parts Y and Z (about 2% of available data): Saharan dust events.

Y difficult to classify, includes dust clouds, classes ($G = 3$ to 6), with also clear scenes, classes ($G = 0$ to 3); F mean: 0.35.
Z reliably classified as Saharan dust clouds, classes ($G = 6$ to 9); F mean: 0.75.

d. Creation of F cloud cover value*

For the points in part A in the s_3–R_{IR} graph, F^* values are obtained by Eq. (14), from d values. For the points in other parts, we allocate representative values to F^*, obtained by comparison with F mean values contained in each part of these (Table 6). This makes it possible to treat the cases (10% of available data) that do not follow the linear criterion of Eq. (14). The frequency of occurrence of these events is noted for each area in 1985, in Table 7.

Let us consider an area with VIS and IR data on a certain period. We calculate s_2, s_3, and R_{IR}. Then, we can obtain Fig. 13, by Eqs. (13), (14), (16), (17), and improvements of Table 7 F^* cloud cover values by our criteria.

e. Comparison between F and F cloud cover*

In case we have F data, it is interesting to compare F^* and F results. We make two sorts of comparison:

Comparison for the 365 days in the year 1985 that we expect a good agreement seeing that we used F values of this year for the "learning" of the D1 method giving F^* values.

Comparison for other months to confirm our method with F data not used in the learning (January 1984, 1986 and July 1983, 1984, 1986).

Note that the F^* values contain information about time slots $(c - 1)$ and $(c + 1)$ by s_2 in the expression of distance d [Eqs. (8) and (13)]. For the comparison with F, we can consider the F values at central time slot c or a mean of F values at time slots $(c - 1)$, c, $(c + 1)$ with weights 1/4, 1/2, 1/4, respectively. The difference between results obtained by the two methods is very slight.

1) COMPARISON FOR VALUES ON SHORT PERIODS

For the first comparison, we plot F and F^* values, versus day, for the year 1985, in Fig. 14, for two areas (area 12, Ouargla, in Sahara, and area 40, Windhoek, in Namib–Kalahari). In Fig. 15, we plot the difference $F^* - F$ for the same two areas. The graphs for daily results being difficult to read, we show graphs for the mean values on 5-day sliding periods. We see a good agreement: the difference between F and F^* is usually below 10%. For the second comparison, we consider F and F^* values, versus day, for January and July, from July 1983 to July 1986. We plot, in Fig. 16, this value for an area in the Sahara (area 12). Here too, we see a good agreement.

We see in Figs. 14 and 16 that for Sahara, in the very warm season (July, August, September) when the F and F^* values are less than 10%, the D1 method (F^* values) gives quantities always slightly less (2%–5%) than C1 data (F values). We guess that, in this case, F values (never equal to 0, but around 2% or 3% in the clearest cases) slightly overestimate the cloud cover (Rossow et al. 1988): conventional meteorological measurements (Capderou 1988) show that in the Sahara, in this season, sky is often absolutely clear (cloud cover equal to 0) over great surfaces.

2) COMPARISON FOR MONTHLY VALUES

We note F_{mon} and F^*_{mon} the monthly means of F and F^*, respectively, daily values defined above. We have very good agreement (Fig. 17). If we plot monthly values for each month, each area, we see a strong correlation between F_{mon} and F^*_{mon} (Figs. 18 and 19); this correlation weakens for large cloud cover, and for the Sahelian region that is not true desert. This shows certainly the limits of the D1 method: this method, based on BDRF ratio defined by Eq. (6), gives good results if the shortwave anisotropic function R, defined by Eq. (3), stays the same in time for a given area: this does not occur for important cloud cover over desert zones, or for the Sahelian zone (desertlike in dry season, land with vegetation in wet season).

3) COMPARISON FOR ANNUAL VALUES

We note F_{ann} and F^*_{ann}, the annual means of F and F^*, respectively.

For annual values, we have also a good agreement between F_{ann} and F^*_{ann} (Fig. 20). The maps (Fig. 21) show the good agreement between the annual means F_{ann} and F^*_{ann} for each area.

Comparing results for the three time scales, we note great improvement in agreement between results of the two methods as we go from daily to monthly to annual mean values. The differences, which can be 10% for the daily mean values, tend to vanish for monthly means, which are well correlated. We note, however,

systematic geographical differences (Fig. 18). Compared to F_{mon} (C1) we find that F^*_{mon} (D1) is practically the same for the Arabian Desert and for Namib–Kalahari (Fig. 19); slightly lower for Sahara; slightly higher for Sahel. For annual mean values, the correlation is even better, but the same geographical differences appear (Fig. 20). One source of the excess of F^*_{mon} for the Sahel could be relatively high values of s_2 (and thus d) for clear scenes. These could arise from departures of the reflectance ratios $D_{i,p}$ in the various desert areas and zones, from spatially homogeneous values D_i corresponding to the angular model assumed to represent *all* clear desert scenes. We note that on both maps of F_{ann} and F^*_{ann} (Fig. 21), the border between Sahara and Sahel appears clearly around isoline 36%.

5. Conclusions

We have shown that cloud cover over dry regions of the Meteosat disk can be estimated in any season, using a simple "distance" criterion in a plane whose coordinates are the relative spatial heterogeneity parameters of the normalized albedo s_2 and of the midday infrared window radiance s_3. In addition, normalizing midday IR window radiance to the maximum value observed over a 10-day period yields an effective criterion (R_{IR}) for detecting Saharan dust or overcast homogeneous cloud cover situations. Comparison of the results with those of the more elaborate ISCCP C1 algorithms shows excellent agreement in detecting cloud-free areas. Agreement in cloud cover is best over true desert regions and remains fairly good over other semi-arid and arid land areas where clouds are more frequent.

Acknowledgments. We thank Geneviève Sèze for useful discussions about ISCCP, and we are grateful to a referee for perceptive comments that helped to improve the paper.

REFERENCES

Capderou, M., 1988: Atlas Solaire de l'Algérie (Tomes 1, 2, 3). Office des Publications Universitaires, Algiers, 1752 pp.

Courel, M. F., R. S. Kandel, and S. I. Rasool, 1984: Surface albedo and the Sahel drought. *Nature,* **307,** 528–531.

D'Almeida, G., 1986: A model for Saharan dust transport. *J. Climate Appl. Meteor.,* **25,** 903–916.

Koepke, P., 1982: Vicarious satellite calibration in the solar spectral range by means of calculated radiances and its application to Meteosat. *Appl. Opt.,* **21,** 2845–2854.

——, 1983: Calibration of the visible channel of Meteosat 2. *Adv. Space Res.,* **2,** 93–96.

Legrand, M., J. J. Bertrand, M. Desbois, L. Menenger, and Y. Fouquart, 1989: The potential of infrared satellite data for the retrieval of Saharan-dust optical depth over Africa. *J. Appl. Meteor.,* **28,** 309–318.

Rossow, W. B., 1989: Measuring cloud properties from space: A review. *J. Climate,* **2,** 201–213.

——, L. C. Garder, P. J. Lu, and A. Walker, 1988: International Satellite Cloud Climatology Project (ISCCP) Documentation of Cloud Data. WMO/TD No. 266, World Meteorological Organisation, Geneva, 78 pages + 2 appendices.

——, ——, and A. Lacis, 1989: Global, seasonal cloud variations from satellite radiance measurements. Part I: Sensitivity of analysis. *J. Climate,* **2,** 419–458.

Schiffer, R. A., and W. B. Rossow, 1983: The International Satellite Cloud Climatology Project (ISCCP)—The first project of the World Climate Research Program. *Bull. Amer. Meteor. Soc.,* **64,** 779–784.

Sèze, G., and W. B. Rossow, 1991: Effects of satellite data resolution on measuring the space/time variations of surfaces and clouds. *International J. Remote Sens.,* **12,** 921–952.

Smith, G. L., R. N. Green, E. Raschke, L. M. Avis, J. T. Suttles, B. A. Wielicki, and R. Davies, 1986: Inversion methods for satellite studies of the earth's radiation budget: Development of algorithms for the ERBE mission. *Rev. Geophys.,* **24,** 407–421.

Stum, J., 1985: Conversion des luminances mesurées par le canal visible de Meteosat en luminances sur tout le spectre solaire. Thèse de 3° cycle, Université de Clermont 2, Clermont-Ferrand, France, 80 pp.

Suttles, J. T., R. N. Green, P. Minnis, G. L. Smith, W. F. Staylor, B. A. Wielicki, I. J. Walker, D. F. Young, V. R. Taylor, and L. L. Stowe, 1988: Angular radiation models for earth–atmosphere system. Vol. I: Shortwave radiation. NASA Reference Publication 1184, 147 pp. [NTIS 89N20587.]

Tanré, D., C. Deroo, P. Duhaut, M. Herman, J. J. Morcrette, J. Perbos, and P. Y. Deschamps, 1990: Description of a computer code to simulate the satellite signal in the solar spectrum: The 5S code. *Int. J. Remote Sens.,* **11,** 659–668.

Vovor, M. K. E., 1991: Etude des masses de poussières sahariennes et leur transport à l'aide du satellite Meteosat durant les années 1984 et 1985. Thèse de 3° cycle, Université Nationale de Côte d'Ivoire, Abidjan, Côte d'Ivoire 140 pp.

Wielicki, B. A., and R. N. Green, 1989: Cloud identification for ERBE radiative flux retrieval. *J. Appl. Meteor.,* **28,** 1133–1146.